3-22-2019

Non-Contact Height Estimation for Material Extrusion Additive Systems via Monocular Imagery

Andrew C. Gorospe

Follow this and additional works at: https://scholar.afit.edu/etd

Part of the Other Computer Sciences Commons

Recommended Citation

NON-CONTACT HEIGHT ESTIMATION FOR MATERIAL EXTRUSION ADDITIVE SYSTEMS VIA MONOCULAR IMAGERY

THESIS

Andrew C. Gorospe, Capt, USAF

AFIT/GCS/ENG/19M

DEPARTMENT OF THE AIR FORCE
AIR UNIVERSITY

AIR FORCE INSTITUTE OF TECHNOLOGY

Wright-Patterson Air Force Base, Ohio

AFIT/GCS/ENG/19M

NON-CONTACT HEIGHT ESTIMATION FOR MATERIAL

EXTRUSION ADDITIVE SYSTEMS VIA MONOCULAR IMAGERY

THESIS

Presented to the Faculty

Department of Electrical and Computer Engineering

Graduate School of Engineering and Management

Air Force Institute of Technology

Air University

Air Education and Training Command

in Partial Fulfillment of the Requirements for the

Degree of Master of Science in Computer Science

Andrew C. Gorospe, BS

Capt, USAF

March 2019

AFIT/GCS/ENG/19M

NON-CONTACT HEIGHT ESTIMATION FOR MATERIAL

EXTRUSION ADDITIVE SYSTEMS VIA MONOCULAR IMAGERY

THESIS

Andrew C. Gorospe, BS
Capt, USAF

Committee Membership:

Dr. G. L. Peterson
Chair

Dr. B. Maruyama
Member

Dr. D. D. Hodson
Member

AFIT/GCS/ENG/19M

Abstract

Additive manufacturing is a dynamic technology with a compelling potential to advance the manufacturing industry. Despite its capacity to produce intricate designs in an efficient manner, industry still has not widely adopted additive manufacturing since its commercialization as a result of its many challenges related to quality control. The Air Force Research Laboratory (AFRL), Materials and Manufacturing Directorate, Functional Materials Division, Soft Matter Materials Branch (RXAS) requires a practical and reliable method for maintaining quality control for the production of printed flexible electronics. Height estimation is a crucial component for maintaining quality control in Material Extrusion Additive Manufacturing (MEAM), as the fundamental process for constructing any structure relies on the consecutive layering of precise extrusions. This work presents a computer vision solution to the problem of height estimation using monocular imagery as applicable to MEAM.

Acknowledgements

Table of Contents

List of Figures

NON-CONTACT HEIGHT ESTIMATION FOR MATERIAL EXTRUSION ADDITIVE SYSTEMS VIA MONOCULAR IMAGERY

I. Introduction

1.1 Motivation

Additive manufacturing is an ever-growing field of manufacturing techniques that is founded on the layer-by-layer construction of three-dimensional structures. The American Society for Testing and Materials (ASTM) International Committee F42 on Additive Manufacturing Technologies defines it as, "a process of joining materials to make objects from 3D model data, usually layer upon layer, as opposed to subtractive manufacturing methodologies," where synonyms include additive fabrication, additive processes, additive techniques, additive layer manufacturing, layer manufacturing, and freeform fabrication [1]. Additive manufacturing provides many benefits over traditional manufacturing technologies. It lends easy, on-demand customization of unique products and allows designs that were not possible with previous manufacturing techniques [2, 3]; according to National Institute of Standards and Technology (NIST), it is cost effective for manufacturing small batches with continued centralized manufacturing as well as provides improved material and machine costs, build envelope and envelope utilization, build time, energy consumption, and labor costs over previous technologies [4]; and along with innovations in autonomous material discovery, it enables environmental-friendly product design unlike any traditional manufacturing process [5].

Material extrusion is one of seven additive manufacturing process categories, en-

compassing fused deposition modeling and fast filament fabrication, "in which material is selectively dispensed through a nozzle or orifice" [1]. Today, material extrusion systems are highest in demand out of all available additive systems as a result of the success of Stratasys and their fused deposition modeling [2]. Though it affords all of the aforementioned benefits, just as with all additive systems, Material Extrusion Additive Manufacturing (MEAM) introduces its own abundant number of challenges that lead to product degradation.

1.2 Sponsor

This research is sponsored by the Air Force Research Laboratory (AFRL), Materials and Manufacturing Directorate, Functional Materials Division, Soft Matter Materials Branch (RXAS). AFRL/RXAS is highly interested in the optimization of MEAM, as it is their instrument for producing multi-purposed flexible electronics, including photovoltaics used in solar energy panels for unmanned aerial systems and flexible batteries used in pH-level scanners for airmen health meters. More specifically, they aspire to advance the MEAM process by improving their current system's capability of quality assurance.

1.3 Research Topic

The build quality of a product made via MEAM can be defined by its geometrical, mechanical, and physical properties. With respect to real-time control of additive manufacturing, there are correlations between process parameters and process signatures that affect a product's quality. Process parameters are either continuously modifiable (i.e. extrusion rate, toolpath movement, etc.) or predefined (i.e. material properties, nozzle properties, etc.) inputs to the additive system. Process signatures are dynamically changing characteristics, which can be observed or measured (i.e.,

bonding reaction to environment, unknown factors like alien particle obstruction, etc.) or are determined through analytical modelling and simulation [6]. Though some research in online process monitoring and control in metal-based additive manufacturing exists, no research is related to the application of the MEAM process.

As MEAM is distinguished by consecutive layering of extrusions, the height measurement of a single layer is the most fundamental feedback for the quality of a printed structure. Each extruded layer requires a target height to assure the geometrical success of a print, which can ultimately affect its physical and mechanical properties as well. Currently, AFRL/RXAS relies on manual feedback of a touch probe sensor to retrieve height measurements for assessing the quality of prints. The current method for target height acquisition requires one or more initial test prints of a layer by fine-tuning process parameters to realize a target extrusion height. Even if the target height is achieved on the first print, the touch probe mechanism is invasive and has presumably damaged the print with its physical contact. Additionally, this method requires redundant and ultimately excessive labor. Thus, their current solution for the basic quality assurance of MEAM is highly inefficient.

1.4 Research Objective

In order to address the above issues, this thesis presents an alternative solution for extrusion height estimation in pursuance of a non-invasive and man-hour efficient quality assurance process for MEAM additive systems. This study involves multiple stages to accomplish this solution.

This thesis begins by developing a software application for the automation of material extrusion printing. The software provides both manual and automated control of the entire additive system, with an object-oriented design and command-line interface. The goal is to support portability to other additive systems through the use

of various software design principles. It supplies the control-loop feedback necessary to implement the height estimation capability as well as accommodates extensibility for implementation of prospective feedback mechanisms.

Utilizing the software application, an experimental testing phase refines the process and requirements for data collection; the goal is to acquire the information necessary to build a predictive height estimation model. Through iterative modification to the design of the experiment, this thesis develops an automation process for the mass production of extrusions, height information, and imagery data.

The next research objective is to compose an algorithm for extracting height information from the images collected on sample extrusions. This thesis implements the photometric stereo surface reconstruction algorithm to translate two-dimensional images into three-dimensional structures. Then using the samples created in the experimentation phase, this study builds a predictive model for estimating heights of extrusions by correlating the calculated depths to height measurements. The key advancement in this method is that it provides a height estimation mechanism for online feedback during MEAM prints to allow for non-invasive print correction.

1.5 Assumptions and Limitations

Assuring high levels of quality and consistency of MEAM products is a challenging task as a consequence of the very large number of correlations between process parameters and process signatures that affect an extrusion's outcome. These include the high complexity of physical phenomena and transformations that result from part production as well as the lack of formal mathematical and statistical models required to control the build process outcome and ultimately print quality. In attempt to relax some of these complications, some assumptions are made to simplify this study.

This study only considers short, single-line prints of a single material in the xy-

plane. Different materials and structures impose challenges with lighting, camera, and environment configurations, along with print parameters and signatures. This methodology mitigates the complications these introduce at the expense of creating a more robust and practical height estimation tool.

There are assumptions related to utilizing the photometric stereo surface reconstruction method, such as imaging with orthographic projection and surface reflectance properties. Chapter II discusses these in further detail.

This study is constrained to the hardware limitations of the available MEAM additive system and its peripheral devices. Thus, methods chosen are based on the capabilities of the system (i.e. central placed camera, lighting positions, downsampling images, etc.). Additionally, the iterative modification to the experimental design, in tangent to its laborious requirements, limit the quantity and quality of the final data collection.

1.6   Thesis Organization

This thesis is organized as follows: Chapter II discusses relevant literature leading to the understanding of the photometric stereo problem formulation as well as reviews similar attempts to automate control of processes in additive systems. Chapter III presents the final version for the design of experiment, along with the necessary techniques involved with preparing for surface reconstruction. It then discusses the exact methods use to create surface heights and the model designed to predict surface heights from monocular imagery. Chapter IV analyzes the performance and results of the developed algorithm. Lastly, Chapter V provides a summary of conclusions and discusses future research opportunities.

II. Literature Review

This chapter discusses the relevant literature to developing an algorithm for predicting heights of Material Extrusion Additive Manufacturing (MEAM) single-line prints. We explore the evolution of depth perception within the computer vision field leading to the technique chosen for this study, photometric stereo, with the following section covering its problem formulation. This chapter also reviews relevant research in automation of process control in additive systems as well as autonomy in materials research.

2.1 Depth Perception in Computer Vision

The human brain can recognize faces in photographs with variations in illumination, viewpoint, and expression. It is able to interpolate the missing information from a 2D image in order to understand the 3D scene it represents. Researchers have aimed to recreate the human's innate ability to perceive depth ever since the invention of the stereoscope in the 19th Century. The introduction of digital photography empowered the capturing of optical images and storing such images as electrical signals, or digital images. With this, depth perception in the field of computer vision has evolved over the years through a collection of techniques classified within 'Shape-from-X.'

Fundamentals of Light and Images.

Understanding how depth perception is achieved begins with understanding how the digital image is created. A camera captures an optical image via its lens by sensing light reflecting from a 3D scene and then projects the image upon a 2D plane. The optical image is converted to a digital signal by a millions of tiny light sensors, known as photosites, in the camera (i.e. CCD, CMOS, etc.). The size of the digital signal

depends on the quantity of the photons emitted from the scene and captured by the photosites, the bit depth of each photosite, as well as the file format conversion. Each sensor directly corresponds to individual pixels within the final digital image. This process for a black and white image can be seen in Figure 1 [7].
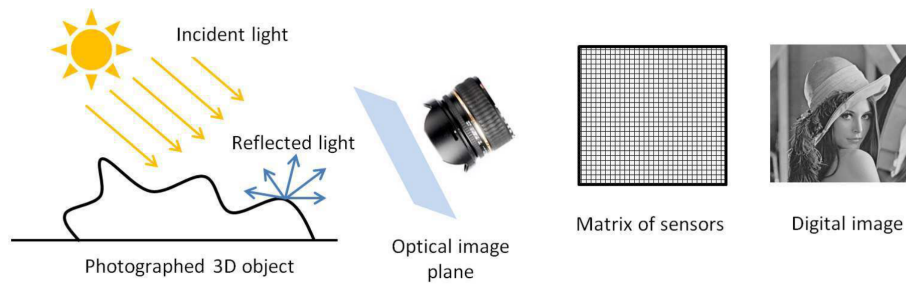
Figure 1. Digital image acquisition process.

As the camera in this study utilizes the Red, Green, and Blue (RGB) format, each photosite has three sensors that only capture the light within the spectrum appropriate to their respective color. Thus, the final digital image is divided into three channels representing the intensity of each color for a given pixel [8]. Utilizing the maximum image size capable of 1044 by 2048 pixels with the high-quality file format Tagged Image Format File (TIFF), the final digital image format is stored as a multi-dimensional array of size 1044 by 2048 by 3 with values ranging between 0 and 255.

Shape-from-X.

The process of achieving depth perception from images using Shape-from-X methods is better perceived as reverse-engineering the aforementioned image acquisition process. The range of approaches studied over the years are generally partitioned into active and passive methods, where each is distinguished by the use of intentional and controlled illumination in a scene or the lack of, respectively [9]. Additionally,

7

each method may utilize single or multiple vantage points. In an introduction to Shape-from-X, Kyrgyzova identifies a few of the most common methods within each category (seen in Figure 2) and provides an overview of those indicated in red [7].
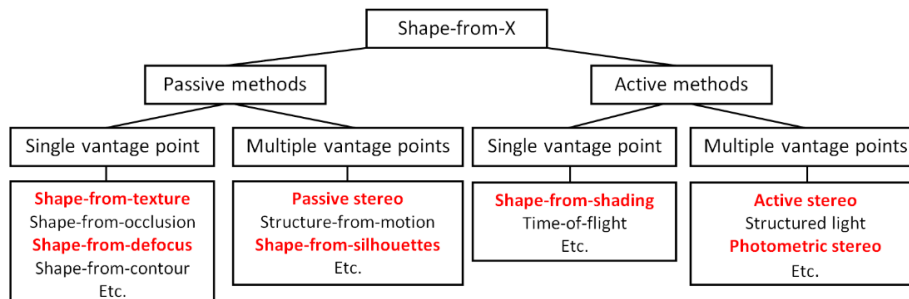
Figure 2. Classification of existing Shape-from-X approaches.

It is widely adopted that generally active methods will provide more accurate surface reconstructions than passive methods when their use is feasible [10]. As the environment of this study was in a lab that allowed the control of illumination projection on still objects, passive methods were not considered. Additionally, the utilized MEAM printer constrained the image collection to a single, centered vantage point. Thus, we consider Shape-from-Shading as the first feasible approach for surface reconstruction. However, today the Shape-from-Shading problem is known to be an ill-posed problem, as a number of studies have shown the solution to not be unique as a result of [11].

There are a number of reasons that the Shape-from-Shading method is infeasible for the surface reconstruction application of this study. Research has shown that when an image of an object with Lambertian reflectance is illuminated by a distant light source and viewed orthographically, there is an implicit ambiguity in determining its 3D structure, which is known as the Bas-Relief Ambiguity [12]. Additionally, the problem formulation requires a number of assumptions that make its use impracti-

cal. The complete list of assumptions necessary for the Shape-from-Shading problem formulation as stated by Klette, et al. are shown in Figure 3 [13].

Shape-from-Shading – Assumptions	
i	The irradiance and the direction of the illumination are known. There are no intra-object or inter-object interreflections. In general, a light source is assumed which emits parallel light of a constant irradiance from a constant and known illumination direction.
ii	The reflection properties of the object surfaces are known. For additional simplification, linearly reflecting surfaces or Lambertian surfaces are often assumed where the albedo is constant and known for the entire object.
iii	The modeling by reflectance maps assumes that a unique scene radiance value is assigned to each surface orientation. Often the reflectance map is assumed to be known.
iv	For the object surface geometry, it is assumed that faces can be approximated by continuous or continuously differentiable functions in classes. Some methods exist which are especially designed to reconstruct polyhedral objects.
v	The sensor is linear.
vi	Shading based shape recovery methods usually assume an orthographic projection of scene objects into the *xy*-image plane.

Figure 3. List of assumptions necessary for Shape-from-Shading.

These assumptions are reduced by extracting parameters from the scene that are expected to be known. This can be done by assuming parallel illumination, Lambertian reflection, and constant albedo. Already these assumptions prevent the use of Shape-from-Shading as the surface reflection of Silver Poly(Methyl Methacrylate) (Ag-PMMA) is highly specular. Nonetheless, we progress through the Shape-from-Shading problem formulation in order to gain insight into the method chosen for this study. To do such, we must first realize the properties of light reflectance and its interaction in a scene in order to fully understand why the camera captures the images it does.

Shape-from-Shading.

The premise behind Shape-from-Shading is that the 3D shape of an object can be estimated by using shading in a 2D image. The previous section discussed how

the imaging process is one that maps light intensities from points in a scene onto in an image plane, known as the reflectance map. Understanding the physics of how light reflects from surfaces enables utilizing the reflectance map to reverse engineer the imaging process in order to extract the shape of an object. It must be noted that in any surface, one of three behaviors may occur when a surface is illuminated; the light can reflect, refract, or scatter. This study only considers surface reflection.

The irradiance at a point in an image plane is determined by the radiance intensity of the corresponding point in the scene. There are two factors that affect the radiance reflected by the object in the scene. The first is the illumination that falls on that surface, and the second is the amount of incident illumination that reflects from the surface. Typically, the radiance emitted from the surface is calculated using a Bidirectional Reflectance Distribution Function (BRDF). In order to determine the irradiance of an image using the geometry of the surfaces and the light source position, we must know the BRDF for the scene surfaces [14]. Only then can we use the BRDF to calculate the surface normals for each point in the image.
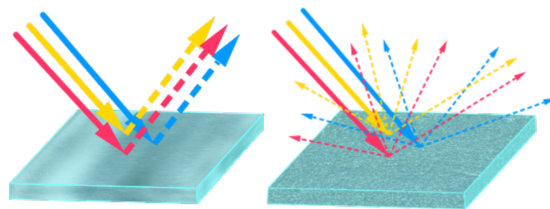
Figure 4. Specular (left) and Lambertian, or diffuse, (right) reflectance.

The appropriate BRDF is completely dependent of the reflection properties of the surface. Of these, there are Lambertian—or diffuse—reflectance, where incident light is distributed in all possible surface directions such that equal energy is seen from any direction, and specular reflectance, where all incident light is illuminated at the same angle opposite the surface normal. Figure 4 portrays these reflectance properties [15].

10

Though it is common to use a combination of both specular and diffuse reflectance to model reflectance properties of an object, as this is most appropriate for real-world applications, the classical Shape-from-Shading problem assumes a Lambertian reflectance.

$$N = N_0 \cos \theta \tag{1}$$

Thus, Lambert's cosine law (Equation 1) states that the perceived brightness of a surface illuminated from a point source is inversely proportional to the angle between the surface normal and the viewing direction [16]. Assuming perfect diffuse reflection, the BRDF simplifies to a constant of $\frac{\rho_d}{\pi} I$ [14], where ρ_d is the surface albedo and I is the source light intensity, which greatly reduces the surface radiance to Equation 2.

$$L = \frac{\rho_d}{\pi} I \cos \theta_i \tag{2}$$

Equation 2 is a formulation for the reflectance map L in terms of scene illumination, surface reflectance, and representation of surface orientation. It can then translate to Equation 5 using vector components in order to solve for the surface normal.

$$L = \frac{\rho_d}{\pi} I \ \vec{n} \cdot \vec{s} \tag{3}$$

Figure 5 depicts each of the components necessary to calculate the radiance of a given point on a Lambertian surface [17]. Given the assumptions made for surface albedo and light source intensity, the known radiance at each pixel and light source direction can now render the surface normals in an image. This is the formulation for the Shape-from-Shading problem.

As mentioned earlier, the Shape-from-Shading method for surface reconstruction is a less than ideal solution for real-world applications as a consequence of the as-
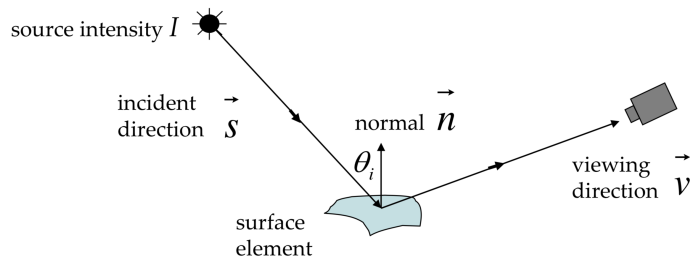
Figure 5. Representation of components in surface radiance.

sumptions it requires. Zhang, et al. provide a broad survey of many approaches to tackle the Shape-from-Shading problem using various optimization techniques, yet the conclusions of each are rather disappointing, as none of the algorithms discussed give satisfactory results [18]. However, photometric stereo, an augmentation of the Shape-from-Shading surface reconstruction method, has shown to provide favorable results on real-world images [19].

2.2 Photometric Stereo

The method chosen for surface reconstruction in this study is the photometric stereo technique, adapted for use on high specular surfaces. In order to realize the problem formulation, the following section walks through the Lambertian photometric stereo method, which assumes a Lambertian surface as it relates to the aforementioned surface reconstruction technique. Additionally, it covers several works that utilize various adaptations to the photometric stereo method and provides rationale for the final method chosen.

Lambertian Photometric Stereo.

Using the information on shading variation, just as in Shape-from-Shading, the photometric stereo surface reconstruction method exploits two or more images from

a fixed camera position along with varying illumination directions per image. Thus, Shape-from-Shading may be considered a special case of the Lambertian photometric stereo method when only one image is used for the surface reconstruction and the surface is assumed to have diffuse reflectance only. It follows then from the reflectance map for all images, the Shape-from-shading problem is a system of equations to solve for the surface albedo and surface normals.

$$
\begin{cases}
I_1 & = \rho_d N \cdot L_1 \\
I_2 & = \rho_d N \cdot L_2 \\
\quad \vdots \\
I_n & = \rho_d N \cdot L_n
\end{cases}
\tag{4}
$$

Equation 4 represents the systems of equations that now relate to a single pixel in the captured images. Equation 4 translates into a matrix equation [20].

$$
\underbrace{\begin{bmatrix} I_1 \\ \vdots \\ I_n \end{bmatrix}}_{I} = \underbrace{\begin{bmatrix} L_1^T \\ \vdots \\ L_n^T \end{bmatrix}}_{L} \underbrace{\rho_d N}_{G}
\tag{5}
$$

If we let G denote the term $\rho_d N$, we can then solve for each surface normal and surface albedo per pixel by solving for G. First, Equation 6 shows the progression for how to manipulate 5 in order to solve for G.

$$
I = LG
$$
$$
L^T I = L^T L G
\tag{6}
$$
$$
G = \left(L^T L \right)^{-1} \left(L^T I \right)
$$

13

G is then solved for using least squares approximation. Finally, solving for the surface albedo (Equation 7a) ultimately provides the solution for the surface normal (Equation 7b) at each pixel.

$$\rho_d = \|G\| \tag{7a}$$

$$N = \frac{1}{\rho_d}G \tag{7b}$$

This is the complete formulation for the Lambertian photometric stereo problem. Now we can use the process of the photometric stereo method in conjunction with more realistic reflectance models to improve the accuracy of the surface normal map.

Specular Photometric Stereo.

Since Woodham's introduction of photometric stereo in 1980 [21], researchers have aimed to improve the surface reconstruction method by extending the fixed viewing, varying illumination across multiple images technique to surfaces with unknown reflections, as most real surfaces are neither purely Lambertian nor perfect mirrors.

There have been many works over the years to handle specular reflection in photometric stereo. Ikeuhi was the first to apply photometric stereo to specular surfaces with his use of three light sources, each with its own reflectance map, in the form of lookup tables [22]. He continued his work with Nayar, et al. by creating a 'photometric sampling' technique to calculate the surface orientation as well as both components for diffuse and specular reflectance [17]. By applying nonlinear regression techniques to a simplified Torrance-Sparrow reflectance model, Kay and Caelli introduce a simulated annealing algorithm to simultaneously estimate the surface normal and surface roughness [23]. Also utilizing the Torrance-Sparrow model, Georghiades demonstrates how to resolve inherent ambiguity in uncalibrated—unknown light source positions—photometric stereo for a large number of non-Lambertian surfaces by solving for

14

reflection coefficients, surface normals, and light intensities and positions through an iterative nonlinear optimization process [24]. Shen, et al. create a novel procedure by first solving for the specular coefficients and then using these to estimate the diffuse reflectance and surface normals [25]. Chung and Jia calculate normals and BRDF parameters for shadow points by using the Ward reflectance model and cast shadow information [26]. Khanian, et al. target eliminating orthographic projection and Lambertian surface assumptions in common photometric stereo techniques by utilizing perspective projection and the Blinn-Phong reflectance model, the reflectance model chosen for this study [15].
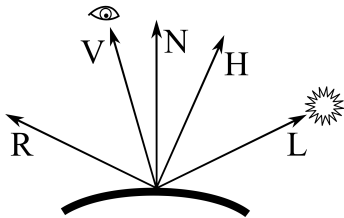
Figure 6. The Blinn-Phong illumination model.

The Blinn-Phong model is Blinn's [27] slight modification to the original reflection model introduced by Phong [28] in 1975. Today, it is widely adopted in the synthesis of modern computer graphics, which is why it was chosen for this study. The Phong model was novel in that it created a more realistic lighting model by introducing a specular component, creating an additional term in the BRDF. However, Phong's model contained a minor computational error that did not account for situations where the reflection and view directions were greater than 90 degrees. Thus, Blinn modified the model by creating an additional 'Half-Angle' vector, which is the vector halfway between the viewing and light position vectors (Equation 8).

$$\vec{H} = \frac{\vec{L} + \vec{V}}{\|\vec{L} + \vec{V}\|} \tag{8}$$

Now, using the Blinn-Phong reflectance model, Equation 9 becomes our reflectance map for which we can calculate the surface normals.

$$I = \rho_d \left(\frac{L \cdot N}{\|L\|\|N\|} \right) l_d + \rho_s \left(\frac{H \cdot N}{\|H\|\|N\|} \right) l_s \tag{9}$$

In the same manner as discussed for Lambertian photometric stereo, Equation 9 can be transformed into matrix form and then photometric stereo for specular surfaces becomes a system of equations to solve for the surface normals at each point in the images.

2.3 Depth Estimation

Depth estimation in computer vision literature is most often found associated with the problem of stereo vision and its variants, as a disparity between two or more images of an object allows triangulation of epipolar geometry to obtain its surface and relative depth [29]. Other techniques, such as vergence, stereo matching, defocus cue, familiar size, and combinations of each are also popular applications to extract depth from imagery [30]. In more recent literature, studies have shown success with both supervised and unsupervised deep learning methods by utilizing convolutional neural networks to extract features relevant for depth cues in an image [31]. Though it is more common to find applications of using depth—typically from range imaging—to estimate or enhance surface normals of an image, depth can be estimated from surface normals with a strong understanding of image projection in gradient space.

Gradient Space.

Macworth first introduced the concept of gradient space in order to capture the relationship between surface orientation and image intensity [32]. Gradient space begins with defining the surface height at each pixel location z as a function of its

image coordinates (x, y) (Equation 10).

$$-z = f(x, y) \tag{10}$$

Under the assumption of orthographic projection, the surface gradient at each coordinate is defined by taking the partial derivative of each surface height with respect to its image coordinate (Equation 11).

$$p = \frac{\delta z}{\delta x} \quad q = \frac{\delta z}{\delta y} \tag{11}$$

Now, all such points p and q lay on the pq-plane known as the gradient space, since every point corresponds to a particular gradient. Each distance of a point (p, q) from the gradient space origin signifies the slope of the surface at that point and the direction is the direction of steepest ascent [33]. This function maps each normal of the surface to a point in gradient space. In other words, at each point on a surface, the projection of that surface normal intersects in gradient space at point (p, q). Thus, Equation 12 defines the surface normal as a vector in gradient space [34].

$$n = [p, q, -1] \tag{12}$$

Depth from Normals.

The photometric stereo method discussed in Section 2.2 resulted in defining an object in an image as a collection of normal vectors representing the surface orientation direction at each point in the image. The goal of depth estimation from surface normals is to define an object in an image as a collection of relative depths—or heights—from the image plane. With the definition of the surface normal in terms of gradient space (Equation 12), we can derive an estimated depth as the components

p and q are the first partial derivatives of depth z. Thus, the map of surface depths must minimize Equation 13.

$$\iint (z_x - p)^2 + (z_y - q)^2 dxdy \tag{13}$$

Ikeuchi suggests using Euler's differential equation method to solve this calculus of variation problem,

$$\nabla^2 z = p_x + q_y \tag{14}$$

which leads to the simple iterative scheme below.

$$z^{n+1} = \bar{z}^n - \rho(p_x + q_y) \tag{15}$$

Here $\bar{z}$ is the local average depth of a region of depths and ρ is the parameter for the method in how the average is computed over a connected region [35]. Thus, using the normal map obtained from photometric stereo, Equation 15 can derive the map of relative depths, or the depth map.

2.4   Autonomy and Automation of Additive Systems

The advent of additive systems introduced a new paradigm for producing arbitrarily complex geometries, such as intricate internal features, lattice and honeycomb structures, etc. for metal-based products. Achieving high levels of quality and repeatability when using additive systems to make metal parts has been a challenging task due to lack of development in process control for additive systems. The following section demonstrates a few recent advances in the evolution of automation and process control in additive systems for the production of metallic products. It concludes with a review of recent developments in autonomy for materials research.

Automation and Process Control of Additive Systems.

Powder Bed Fusion (PBF), the additive manufacturing process in which thermal energy selectively fuses regions of a powder bed, and Directed Energy Deposition (DED), the additive manufacturing process in which focused thermal energy is used to fuse materials by melting as they are being deposited, are the two most commonly used process categories for creating metallic products [1, 36]. The earliest efforts for process control of PBF begin with the commercial laser-based process, Selective Laser Sintering (SLS). Melvin III, et al. construct a video microscopy system to provide insight on powder flow behavior and improve the quality of the sintering process in general [37]. Several authors extend this research further. Berumen, et al. use a digital camera to monitor the powder coating step for each layer and create algorithms to detect low or excessive powder feed and coater problems [38]. With the aid of subsequent image processing, Kleszczynski, et al. create a system using a high-resolution Charge-Coupled Device (CCD) camera mounted outside the build chamber that is able to detect errors in process stability (i.e. insufficient powder, poor supports, coater damage, etc.) and part quality [39]. Using a Complementary Metal-Oxide Semiconductor (CMOS) camera and a photodiode coaxially to the laser beam, Kruth, et al. and Surreys, et al. design and patent a feedback control system, perform experiments on parts with complex features, and test different combinations of scanning patterns [40, 41]. Using this patented system along with a high-speed CMOS camera and a photodiode, Craeghs, et al. build a feedback controller for laser power and use it to test part quality in special geometries, like adjacent scan vectors, overhang, down-facing structures, and acute corners [42, 43, 44].

DED processes are slightly ahead of PBF processes with regards to real-time process control as a result of the variant DED process laser cladding, intended for coating existing parts rather than building 3D components, having been developed

prior to the PBF process [36]. With consideration of the similarity in principle of DED and PBF processes—the main difference being the feed mechanism—research on monitoring DED processes has also primarily focused on temperature monitoring and control. However, a few research efforts have investigated monitoring the height of each layer during fabrication. Iravani-Tabrizipour and Toyserkani use an optical system composed of three CCD cameras, each positioned at 120 degrees slant relative to each other and 15 degrees tilt from the substrate plane, along with a recurrent neural network to measure and monitor the height of each layer during the laser cladding process [45]. Figure 7 depicts their height estimation system.
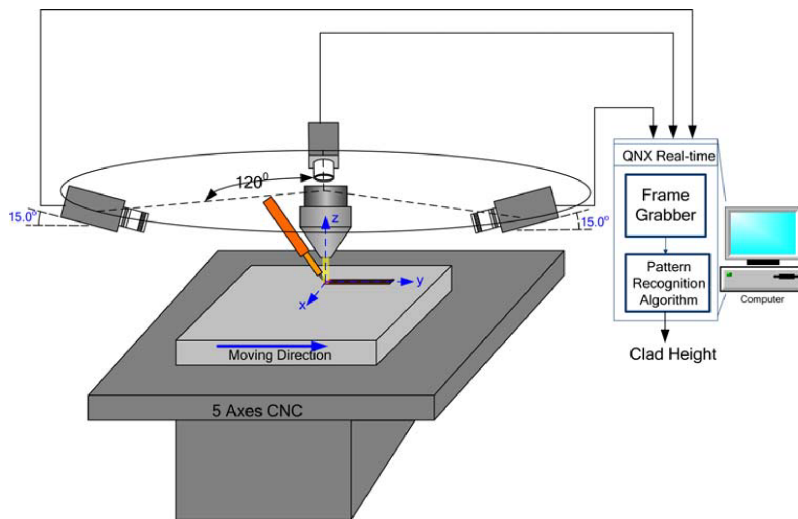
Figure 7. Iravani-Tabrizipour and Toyserkani's optical height estimation system for the laser cladding process.

Song, et al. continue with a similar three camera system to measure height with the addition of a pyrometer to measure the melt pool temperature, creating a monitoring system capable of adjusting the laser power based on height and temperature feedback [46]. Fathi, et al. and Toyserkani and Khajepour propose a different approach for height monitoring and geometry control [47, 48]. They patent a system that uses a

20

single CCD detector mounted normal to the process zone, along with interference and neutral filters, to detect fluctuation in layer heights as well as estimate the roughness and ultimately quality of a surface [49].

Autonomy in Materials Research.

Additive systems are an engine for the evolution of materials research. In addition to the labor of utilizing additive systems, materials research also demands significant human interaction. Humans facilitate initial hypothesis generation, experimental design, analysis, interpretation and iterative hypothesis refinement. Understanding the relevant phenomena of a given material problem often requires numerous experiments, which slows the research process. The iterative design of experiments requires modification to subsequent experiments based on prior results. Autonomy in materials research serves to eliminate the human labor bottleneck in this iterative learning loop, allowing the exploration of complex experimental parameter spaces.

Nikolaev, et al. spearhead the development of autonomous systems in material research. With the introduction of the Autonomous Research System (ARES), they combine robotics, artificial intelligence, data science and in-situ techniques to vastly expand the realm of materials development. More specifically, they use ARES for the enhancement of single-walled Carbon Nanotubes (CNTs) synthesis. They demonstrate with ARES the ability to traverse a high-dimensional parameter space, varying multiple growth parameters between experiments, to control CNTs growth rate [50]. Their research encourages application to other materials and processes, allowing a fundamental change to the materials research process to overcome more complex and impactful problems.

2.5   Conclusion

Section 2.1 gave a historical background of depth perception in computer vision leading with mathematical support for understanding the Shape from Shading problem. This was then extended to the photometric stereo problem formulation in Section 2.2 to help understand the surface reconstruction and depth estimation techniques used in this study. Section 2.3 covered additional research in autonomy and automation of additive systems, providing patented systems for process control in various additive manufacturing processes other than MEAM and research in autonomous systems for materials research. With consideration of the assumptions and limitations covered in Section 1.5, Chapter III provides the complete algorithm for height estimation developed for the MEAM system provided by Air Force Research Laboratory (AFRL)/Materials and Manufacturing Directorate, Functional Materials Division, Soft Matter Materials Branch (RXAS).

III. Methodology

This chapter describes the methods used to acquire estimated heights from monocular imagery of Material Extrusion Additive Manufacturing (MEAM) prints in order to empower the printer automation control system to provide both single- and multi-layered print correction. The algorithm we build is founded on the photometric stereo computer vision technique, as we use surface reconstruction to create parameters for the estimation model.

First, we develop the automation control system for the additive system to enable both successful data collection and model performance testing. Then we create a dataset through the production of MEAM single-line prints with the capturing of multiple images with varying light source positions and height measurements for each. We then created a linear regression model to estimate height measurements and compare variations in model creation and data collection techniques. We conclude the chapter with discussing the measures taken to prepare the analysis of the model.

3.1 Automation Control System

The automation control system is responsible for complete systematic control of the MEAM additive system. It is a closed-loop feedback control system consisting of sensors and actuator agents. These agents are made up of mechanics elements within the MEAM printing apparatus as well as the standalone computing system that interfaces with the master controller. The printing apparatus and standalone computing system communicate by serial, analog, and digital connections via the master controller. Ultimately, the user has full control of the MEAM printer using Python.

Additive System Architecture.

The MEAM additive system consists of core and peripheral devices. The core devices are critical and must remain fully operational during use of the system. Failure of a core device will result in failure of the entire system and potentially physical harm to the printing apparatus. Peripheral devices are optional for use within the additive system and provide supportive functionality.
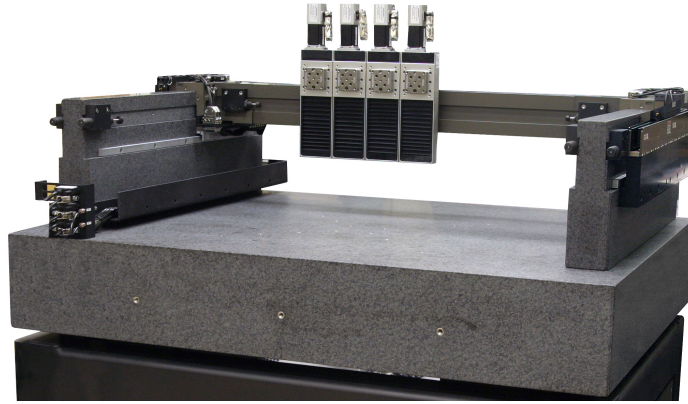
Figure 8. The MEAM printer gantry subsystem.

The core devices of the additive system include the gantry subsystem, the extrusion subsystem, the master controller, and the computing system. The gantry subsystem consists of the mechanical components that provide three-dimensional motion to the additive system (Figure 8). It is comprised of a single arm providing movement along the x-axis resting above two slaved arms providing movement along the y-axis. Resting along the x-axis arm are four miniature arms controlling movement in the z-axis. All movement is enabled by powered magnets with resistance controlled by pressured gas. The extrusion subsystem is comprised of a pump that controls the extrusion rate of a material as well as the nozzle, nozzle tip, and nozzle connection. The nozzle tip size selected for the experiments performed in this study is 0.25mm in diameter. The master controller ultimately controls the aforementioned core com-

ponents through serial, analog, and digital communication. Additionally, the master controller commands the operation of some peripherals devices. Finally, the last core component is the computing system, which provides a human interface to the master controller as well as the operation of peripheral devices not interfaced through the master controller.

The peripheral devices of the additive system include the touch probe, camera, and hot plate. The touch probe interfaces through the master controller and provides the capability of measuring printed extrusion heights via physical touch and electrical response. The camera interfaces directly into the computing system and provides optical feedback on printed extrusions via still-frame images. The hot plate is used in standalone and is set to a constant 60 degrees Celsius throughout experimentation.

Software Architecture.

The software design shown in Figure 9 provides control of the many devices that make up the additive system. At the lowest level, each *Driver* interfaces with the master controller and auxiliary devices to provide direct communication to the computing system. Utilizing the drivers, each *Device* provides fundamental control over all core and auxiliary devices. Device functionality is then abstracted to the *Process* layer, where processes may control multiple devices to provide both elemental and combinatorial regulation of the additive system. Finally, the *Apparatus* cumulates all processes and devices into a centralized structure for intuitive control of the additive system through the computing system. With this multi-layered design, the user has complete control over the additive system through interaction with the computing system.

Three drivers connect the software design to the physical hardware for the master controller, camera, and pump. Each *Driver* interfaces with their respective Dynamic-
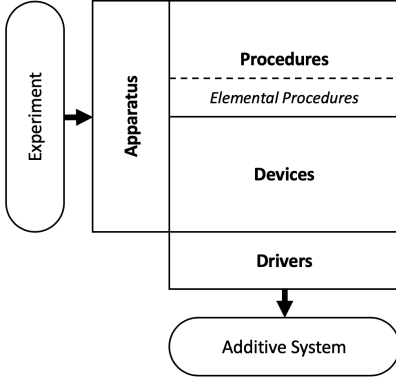
Figure 9. Top-Down software design.

Link Library (DLL) to provide fundamental control of their hardware components. The A3200 master controller *Driver* converts Python language to Aerobasic commands, the proprietary coding language that manipulates the Aerotech gantry subsystem. Examples include getting and setting axes coordinates, providing analog and digital input and output channels, and starting and stopping motion. Additionally, the master controller *Driver* interfaces the Keyence touch probe through the analog input and digital output channels. The camera *Driver* utilizes the `ctypes` Python module to interface with the uEye camera's DLL provided by Imaging Development Systems (IDS). Examples include allocating memory on the computing system to save image captures, executing image captures, and configuring physical gain settings on the camera. The pump *Driver* extends the `serial` Python module to interface the Ultimus V High Precision Dispenser. Examples include setting the pressure and vacuum levels, toggling dispense on and off, as well as getting and setting the vacuum and pressure units. Each driver also provides connection, disconnection, and error handling capabilities.

At the next level, devices abstract the functionality of the drivers. Figure 10 depicts the hierarchical structure of the *Device* class and subclass inheritance. Each device belongs to the *Device* parent class, which contains three subclasses, 'Motion,'

26
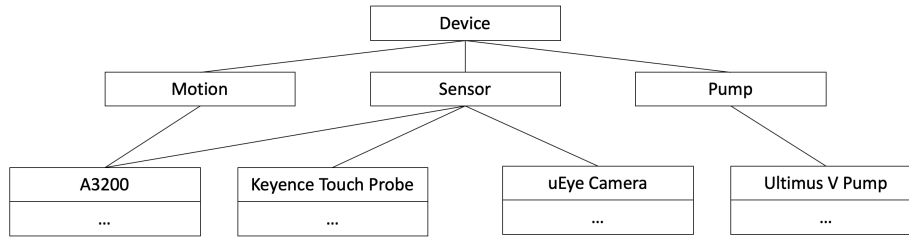
Figure 10. Class inheritance for devices in the software design.

'Sensor,' and 'Pump.' The *Device* superclass (Level 1 in Figure 10) mandates common functionality across all devices (i.e. connect, disconnect, command logging, etc.). Each *Device* category subclass (Level 2 in Figure 10) mandates common functionality for motion, sensor, and pump devices. These category subclasses enable plug-and-play capability for use of the software design on additive systems that utilize different hardware components. Thus, with the development of a device-specific subclass (Level 3 in Figure 10) and a corresponding driver, any appropriate additive system device could be used in this software design.

The remaining levels of the software design provide abstracted authority over the additive system. A *Procedure* provides iterative sequence control of device functionality. With any given action, the additive system may require use of multiple devices. The distinction between elemental and regular procedures is that of complexity; elemental procedures are simple procedures that occur most often. The *Apparatus* is the software equivalent of the entire additive system. It provides the user complete control of the additive system through combination of procedures, elemental procedures, and devices—the user does not have access to drivers. Though a user does not need an *Experiment* to control the additive system, the *Experiment* provides automated control of the *Apparatus*. Thus, we use an *Experiment* for to collect the data we need to develop a height estimation model.

3.2   The Data Collection Process

Utilizing the aforementioned software design, the experimental design is directed towards collecting data that will satisfy the necessary constraints for each analysis technique discussed in Section 3.4. Automation of the additive system allows the printing of samples of Silver Poly(Methyl Methacrylate) (Ag-PMMA) and the gathering of appropriate data on each sample. The experimental design consists of both physical preparation as well as automated control of the *Apparatus* via an *Experiment*. Figure 11 lists the steps covered throughout this section.

Design of Experiment

Preparation (per Collection of Samples)
- Environment Configuration
- Environment Regulation
- Apparatus Calibration

Automation (per Sample)
- Substrate Height Measurement
- Substrate Image Capture
- Extrude Sample
- Cure Sample
- Sample Height Measurement
- Sample Image Capture (per Light Source)

Figure 11. List of steps taken for the collection of data.

Experiment Preparation.

Several measures are taken to fully prepare the additive system to collect the data necessary to preform relevant analysis techniques. First, configuring the additive system allows mass production of single lines of Ag-PMMA with a length of approximately 5 millimeters. Next, regulating the printing environment promotes consistent and reliable outcomes to the quality of each sample. Finally, calibrating the *Apparatus* enables precise control of the additive system with respect to the current printing apparatus configuration and environment.

The apparatus configuration is consistent across multiple trials to create a repeatable experiment. A glass substrate with a size of approximately 2 by 3 inches allows for printing of 50 samples per execution of the experiment. Laminating the surface with a dark-blue chalk spray prepares the substrate for successful background subtraction and regional maxima extraction during the data preprocessing stage. The environment holds the substrate atop a thermal hot plate, set at 60 degrees Celsius, in the center of the printing stage. The additive system utilizes three of the four available z-axis arms, providing nozzle, touch probe, and camera control. To create the Ag-PMMA, silver microflakes are suspended in an anisole solvent via bath sonication. The PMMA is then added to this suspension and dissolution starts by high-shear mixing. The ink is then left for a couple days to finish dissolving. In order to prepare the Ag-PMMA for extrusion, it is high-shear mixed for 1 minute. The nozzle loaded with the prepared material has a tip of size 0.25 millimeter inner diameter and connects to the additive system pump.

The touch probe rests on the second z-axis arm and requires no further preparation aside from calibration. The camera is mounted perpendicular to the printing stage on the third z-axis arm with its working distance, the distance from the plane in focus, set at approximately 93 millimeters. Attached to the camera is a mount providing

	Slant (θ)	Tilt (ϕ)		Slant (θ)	Tilt (ϕ)
(1)	0°	45°	(7)	180°	45°
(2)	0°	60°	(8)	180°	60°
(3)	60°	45°	(9)	240°	45°
(4)	60°	60°	(10)	240°	60°
(5)	120°	45°	(11)	300°	45°
(6)	120°	60°	(12)	300°	60°
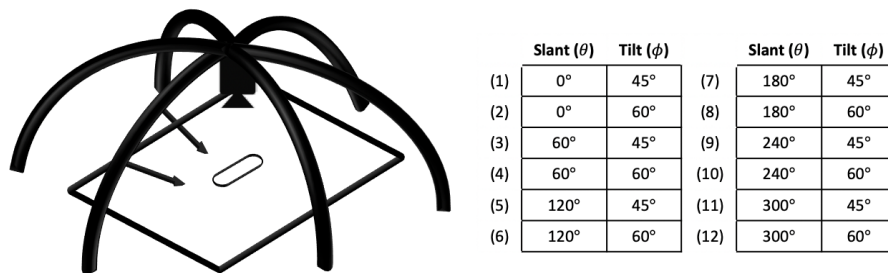
Figure 12. Visual of light source mount (left) and a list of spherical coordinates for each light source direction (right).

29

varying locations for light source placement. Light sources are placed such that the slant and tilt of each light source direction with respect to the substrate surface follow those shown in Figure 12. This configuration covers the optimal tilt of 54.74 degrees, as recommended by Drbohlav and Chantler [51].

The regulation of the environment involves minimizing variables that adversely affect the quality of the data collected. In order to reduce the ambient lighting and consequently strengthen the effect of the directional lighting used, the additive system's integrated lights were disabled. Loose particles (i.e. hairs, dust, etc.) in the printing environment can cause undesired print structure formations by causing build up, blockage, or even smearing of the material extrusion. Thus, prior to every trial, the substrate is thoroughly cleaned using methoxybenzene, or anisole, a readily available solvent known to decrease the viscosity of Ag-PMMA. Additionally, a dump well filled with anisole is added to the printing stage to allow nozzle tip rinsing between printing of samples.

The calibration of the devices in use for the experiment is necessary for each execution of a given trial. This process involves aligning the positions of the nozzle tip, touch probe, and camera within approximately 10 microns accuracy. Additionally, the weight of the Ag-PMMA must be calibrated to control precise extrusion within approximately 1 milligram. At the start of every trial, the touch probe is calibrated with the height of the printing stage. Additionally, the center point for each sample location on the substrate's surface is measured in order to provide height correction to each z-axis position. This practice accounts for variability in the substrate surface height. Finally, the camera physical gains are calibrated in order to capture the widest range of values across each Red, Green, and Blue (RGB) channel while avoiding over saturation with consideration of each light direction. Given the material reflection and background absorption, the camera was set with a master gain of 0%, gain on the

red channel of 30%, gain on the green channel of 0%, and gain on the blue channel of 35%. It must be noted that camera gains were manually adjusted and less than optimal settings for each light source angle were chosen in order to satisfy the constant light intensity constraint of the classic photometric stereo technique as mentioned in Chapter 2.

Sample Collection.

The software implementation of the experiment automation control sequence begins with defining the *Apparatus* to follow the aforementioned printing apparatus configuration. Upon completion of the aforementioned calibration steps, the data collection commences. The following steps loop over all 50 samples per trial. First,
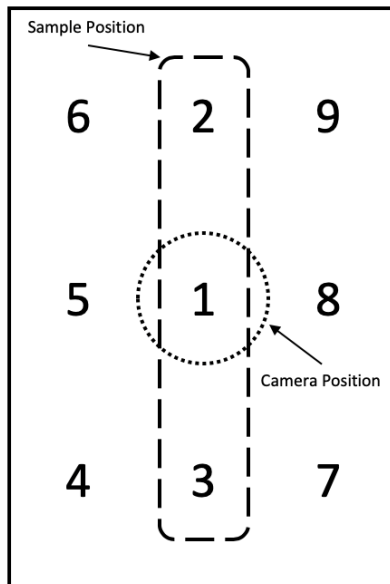

Figure 13. Series of height measurements taken by order.

nine height measurements are gathered via the touch probe, following the progression shown in Figure 13, on the empty substrate for each sample's projected location. Additionally, images are captured at each projected sample location in the first light

source position (θ=0,ϕ=30). Next, the lines are printed using the cleanse-print cycle previously mentioned. Print parameters vary across the xy-grid of samples.

In the x-direction, the nozzle tip height increases and in the y-direction the nozzle trace speed increases, where tip height is the distance between the nozzle tip and the substrate surface at extrusion and trace speed is the movement speed of the nozzle. As the target height of each sample remains constant at 10 microns and the extrusion rate of dispense, or pressure, remains constant at 200 P_{atm}, the variation in tip height results in varied print speed to produce the target wet print height. These varying parameter settings, along with environment differences at time of print, deliver a variety of print outcomes resulting in a collection of unique samples. Upon completion of printing the samples, the system waits five minutes to allow the extrusions to cure. The dried print height differs from the target wet print height depending on the volume fraction of solids in the material ($\approx$ 24 %) and other factors relating to how it cures. Then using the progression from Figure 13, height measurements are gathered for each sample. Finally, high-resolution RGB images (1044 by 2048 pixels) are captured for each of the light source positions according to Figure 12.

Raw images and height measurements were captured for over 500 samples across 12 trials. Many samples were discarded due to structural damage as a result of the wide spread of printing parameters. Additionally, modification of the data collection process resulted in the removal of samples from earlier trials. After removal of a few samples due to image preprocessing failure, the total data collection comprises of 187 samples.

3.3   Data Preprocessing

The data preprocessing phase involves preparing the data for the photometric stereo surface reconstruction method. Image processing and extrusion height extrac-

tion is performed to reduce noise in the input parameters and define target values, respectively. Additionally, the images are downsampled to reduce the computational complexity of the analysis technique.

Image Processing.

As the input images are RGB and have a height of 1044 pixels and a width of 2048 pixels, the raw data begins with a dimension size of (1044, 2048, 3). To remove background noise from each image, masks are created to extract the foreground of each image and thus highlighting the pixel region of interest for each image. Starting
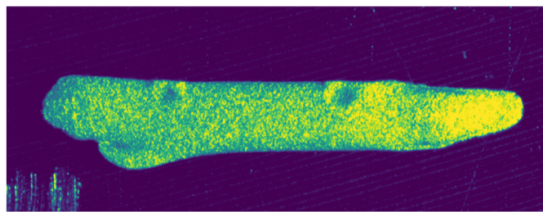
(a) The original image is converted to grayscale and cropped to remove excessive noise.
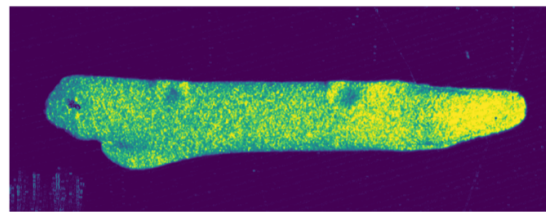
(b) The absolute differential is taken from the the foreground and background image captures.
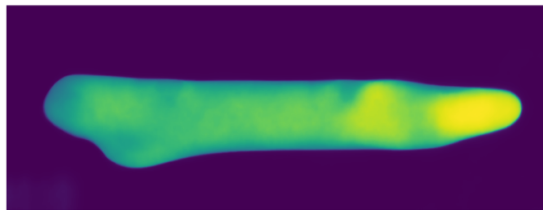
(c) Median and disk filters smooth the sample's rigidity and noise in the background.

(d) The contour of the sample is extracted via binary adaptive and bitwise-NOT thresholds.

(e) The mask is calculated after closing the contour, removing small objects, and filling holes.
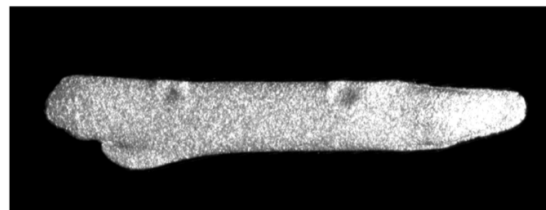
(f) The mask is applied to the original image to superimpose the sample on a black background.

Figure 14. Intermediate phases of the image processing task.

with a collection of six images—one for each light source position—mask generation begins with converting the images (both empty substrate and printed extrusion) at the first light source position (θ=0,ϕ=45) to grayscale by taking the average of all three channels. We then crop the image region of interest to remove excess background noise. Then the absolute differential is calculated between the printed extrusion image and the empty substrate, effectively removing predominant artifacts and substantial noise. The mask is then generated after using a combination of median and disk filters as well as binary adaptive and bitwise-NOT thresholding on the absolute differential. Figure 14 displays the results of each of these steps. Each of the images are then resized to half of their original resolution to reduce computational complexity for surface normal and depth calculations and ultimately increase the efficiency of the height estimation algorithm. Finally, background is added to create a square aspect ration. Thus, a final image has a dimension size of (545, 545, 3).

Height Extraction.

The goal of the height extraction step is to define three extrusion heights from the total of 18 raw height measurements. Because touch probe measures with a precision of 10 microns and at that level of accuracy, the substrate is an asymmetrical surface, three rows of measurements are taken to calculate the average height of the lower and upper bounds of the printed extrusion. As seen in Figure 13, the printed structure covers probes (1), (2), and (3). For the empty substrate measurements, these probes are marginally different from the measurements gathered at their corresponding outer probes and define the lower bound of the extrusion. For the second set of touch probe measurements, the printed structure probes will have a several micron increase, with quantity depending on the structural outcome of the print, defining the upper bound of the extrusion. Once the upper and lower bounds of the extrusion are defined,

three height measurements are defined by taking the absolute difference between the bounds. Additionally, the average height of the extrusion is also saved for single target evaluation.
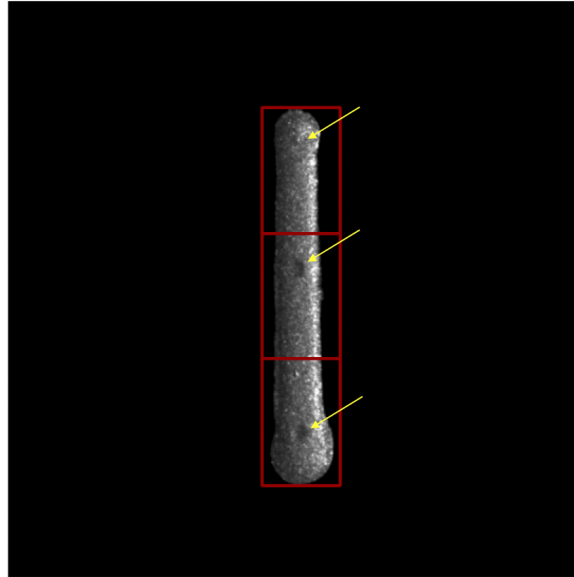
Figure 15. Visual of the region bounds for each sample with indications of touch probe imprints.

A limitation of this study is that the touch probe measures imprecise regions of the extrusion in the $x - y$ plane. For any given sample, the three heights calculated are assumed to be located along the extrusion's center x-point and at the center y-point for each third of the extrusion. Figure 15 depicts a sample split into three regions and portrays the limitation of this assumption, where the visible touch probe imprints from height measurement contact are not located in the center of each region. The location of each touch probe contact on the line varies by sample as a result of the automation of collecting 50 varying samples per trial. Additionally, the heights calculated are assumed to be the maximum height at each point measured, which despite the efforts of curing, is not necessarily the case as the touch probe will return the height measurement of the bottom of the imprint from the probe tip.

3.4   Height Estimation Algorithm

Per discussion in the previous chapter, we use the well-studied computer vision technique of photometric stereo in order to recreate the three-dimensional scene captured in a two-dimensional image. First, we calculate the surface normal for each pixel of every sample. Then using the surface normals we calculate an estimated depth for the regions corresponding to the touch probe measurement locations. Finally, we use these regions of depth measurements as parameters for a linear regression model in order to predict heights from images.
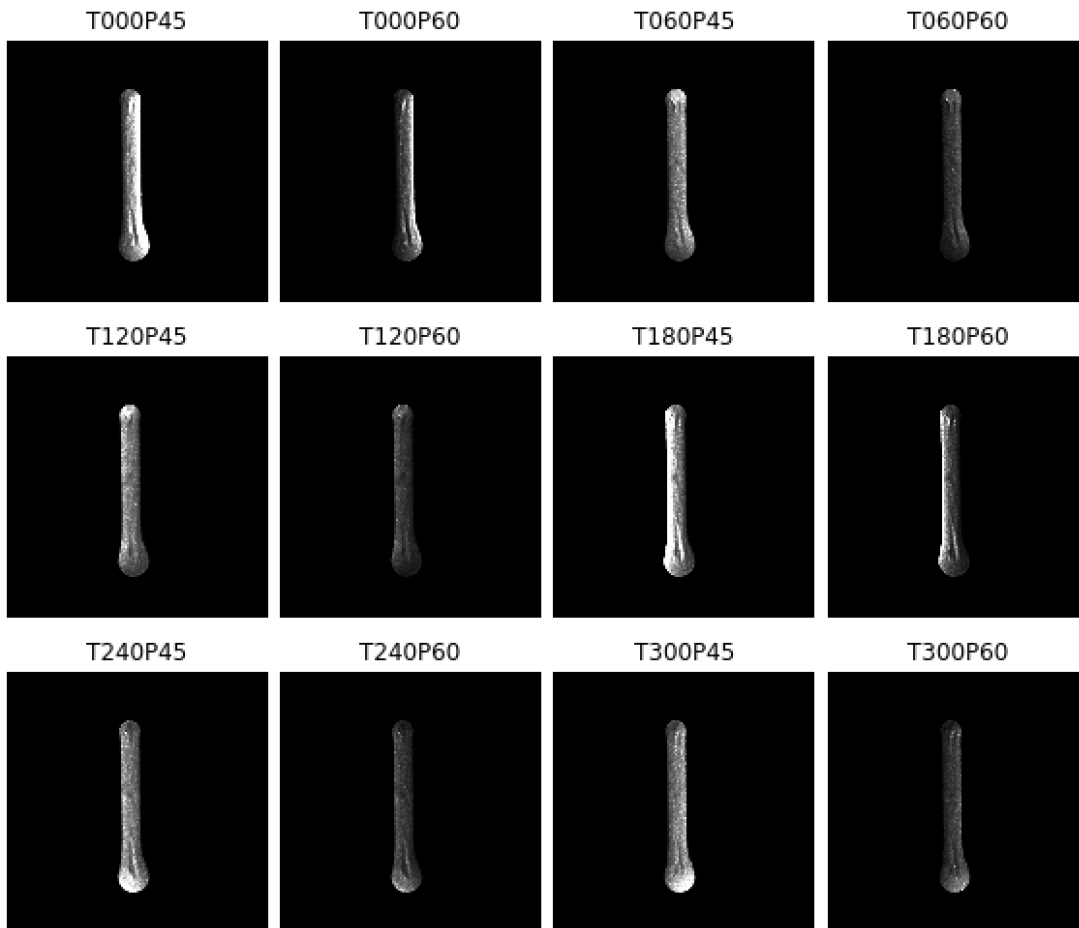
Figure 16. 12 images labeled by degree of slant (T ≔ θ) and tilt (P ≔ ϕ) for their corresponding light source direction for a single sample.

Photometric Stereo and Depth Estimation.

The photometric stereo algorithm starts with 12 preprocessed images, each image captured with the light source positions indicated in Figure 12. Figure 16 shows each of the 12 preprocessed images corresponding to their labeled light source direction. Using the image irradiance equation for the Blinn-Phong model (Equation 9), least squares approximation allows the computation of the surface normals and albedos for each pixel coordinate.
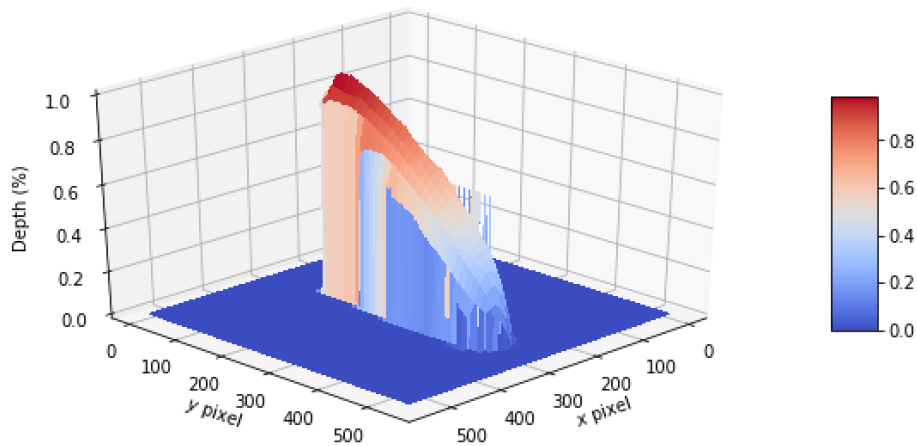
Figure 17. A contour plot showing the full depth map of a sample.

Then using Equation 15, the surface normal map is converted to a depth map. Recall that Equation 15 requires an iterative process of using the average depth for a region of connected points. Several methods were tested to include using solely vertical neighbors and solely horizontal neighbors. After quality checking the results of each, a combination both vertical and horizontal neighbors starting with the surface normal's most center coordinate showed on average a more accurate 3D structure true to sample's surface. As depth's are relative distances to the lowest point in the image, structural integrity as a result of each method were compared by human evaluation. Using the same sample from Figure 16, Figure 17 portrays a contour plot of the

depths calculated for the entire extrusion surface.

As each sample has three measured heights (Figure 15), which indicate truth data for each extrusion, the depth map is also split into three regions and then averaged to return three discrete measurements of the sample's depth. However, the area for each region is restricted by a quarter of the longest dimension of each region. This technique is chosen to remove excessive falloff at the sample's boundaries and consequently produce a more accurate depth average for each region of the sample.

(a)   (b)
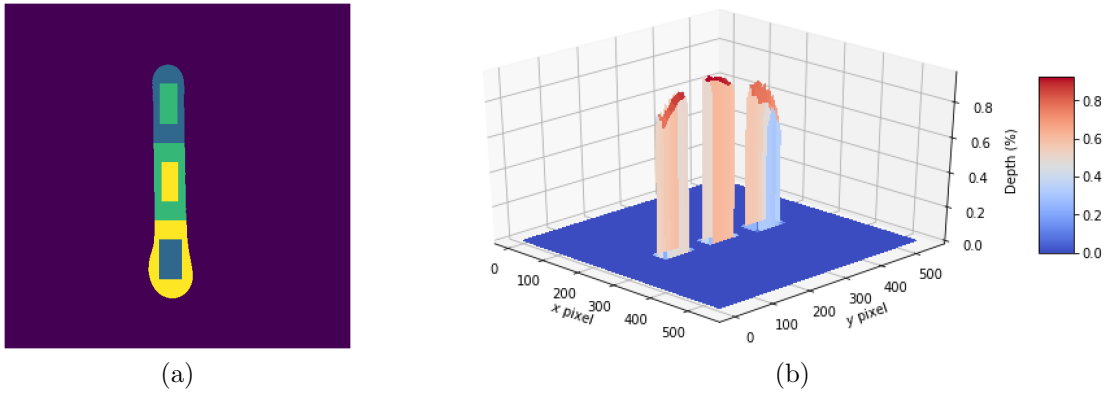
Figure 18. A mask image depicting the region coordinates for each average depth measurement (a) and the application of that mask to the sample's depth map (b).

Finally, the average of each region is saved along with its respective touch probe measurement to give each sample three data points: a measured height and an estimated depth per region.

Prediction Model.

Thus far, the height estimation algorithm is able to correlate depth values from the calculated depth map to the true height values measured via touch probe. In order to create a predictive model, the data points collected thus far are used in linear regression model. Although up to this point there are 561 data points (187 samples × 3 data points per sample), the upper and lower region data points are discarded for

each sample. This decision results from the inconsistent touch probe measurement accuracy due to the automation of the data collection process. Consider Figure 19.
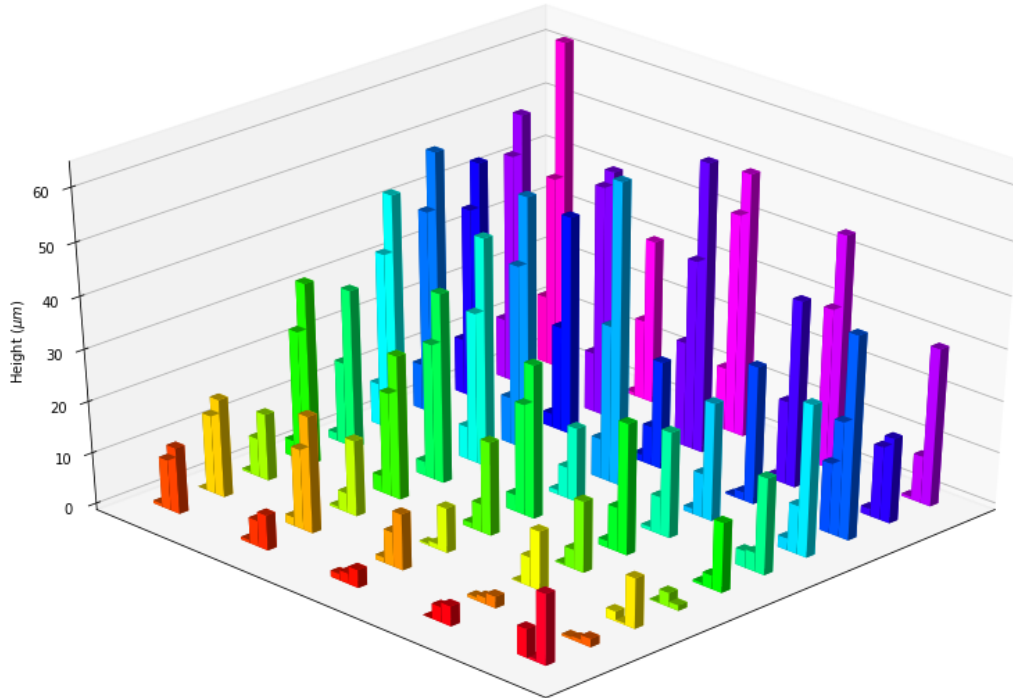
Figure 19. 3D bar chart representing an entire trial of samples height measurements via touch probe.

Though generally the height measurements show a pattern of decline from the start of a printed extrusion to its finish, there are frequent cases of deviation from this pattern. Additionally, almost all depth followed the structural patterns of those shown in Figure 20. These commonalities in depth map structures do not always align correctly with the pattern of the height measurement patterns. Thus, to minimize such disorientation and inconsistency, only the data points for the center point height measurement and depth calculation are entered into the final dataset for the prediction model. Chapter IV provides further analysis and implications of this manifestation.

The 187 observations are split into a nontest and test dataset by 80 and 20 per-
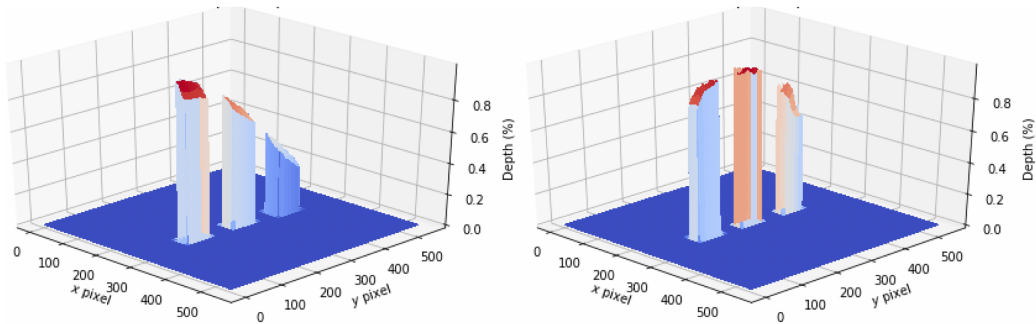
Figure 20. Examples of common cases of depth map structures across sample set.

cent, respectively. Thus, the nontest set consists of 149 observations and the test set consists of 38 observations. Using a k-fold cross validation technique on the nontest dataset, a polyfit transform method allows evaluating multiple linear regression models. A small dataset enables quick testing of numerous models. Polynomials to the degree of 8 are evaluated using ten different training/test splits, controlled by regulating the random state seed. Models are compared by lowest Mean Squared Error (MSE) and the highest performing model is selected.

Using the selected model, the model is evaluated by various statistical measures, to include an Analysis of Variance (ANOVA) report. Chapter IV provides analysis and discussion of the model's performance. Finally, the model is saved and integrated into the height estimation algorithm. The height estimation algorithm is then prepared for integration into the MEAM additive system's computing system to support online prediction of estimated heights via imagery.

3.5   Summary

Software is developed for the mass production of samples to be used for analysis via the designed height estimation algorithm. The data necessary to create and refine the algorithm is collected and preprocessed. Photometric stereo is used to

create a three-dimensional reconstruction of the extrusions, depth is estimated for each extrusion using the surface normals, and a linear regression model is created to predict estimated heights.

IV. Results & Analysis

This chapter provides the results and analysis of the height estimation algorithm for the Material Extrusion Additive Manufacturing (MEAM) system. Each method used to design the algorithm is assessed and critiqued. First, we review the software design and assess based on common software design criteria. Next, we evaluate the efficacy of the experimental design and data collection as well as the preparation of the data. Then we examine the photometric stereo and depth estimation methods and critique for improvement. Finally, we survey the resulting sample population and review performance and results of the predictive height estimation model.

4.1 Software Design Review

Though the design lacks formal requirements, usability and utility were primary concerns for the development of the software design, as well as maintainability for its intended longevity. Deraman and Layzell define primary and secondary categories of criteria for producing maintainable software. The intent of their criteria is to reduce the effort for understanding the software, reduce the effort for corrective maintenance of the software, allow software to accept changes in the future, and promote simplicity of maintenance tasks [52]. The following section reviews the software design for the MEAM system and estimates compliance with each of Deraman and Layzell's groups of software design criteria for maintainability.

Primary Criteria.

Real-world modeling, independence of specification modeling, explicitness, and modularity help determine the ease of adaptive maintenance throughout the software's lifetime [52].

- *Real-world modeling:* The software design anticipates current and future requirements by utilizing a real-world model. The software architecture embodies the additive system's architecture. Through object-oriented design and hierarchical control, it contains driver and device classes that directly mirror the MEAM system's functional flow.

- *Independence of specification modeling:* As no written requirements are provided, no concrete models for specification are created for the software design. However, each of the specification models influence decisions made for the software design. For example, the process and entity models are contained within the software architecture (Figure 9), and task and human-computer interface models manifest with the *Apparatus* class through the command-line interface.

- *Explicitness:* Not every decision in the development process is formally stated and explicitly recorded. This is a shortfall in the software development process likely due to the informality of design requirements.

- *Modularity:* The software design is highly modular as the hierarchical architecture promotes functional decomposition. Additionally, the object-oriented paradigm promotes abstraction, encapsulation, and inheritance, all of which increase the software's flexibility.

Secondary Criteria.

Data dictionary, uniformity, prototyping, user involvement, documentation, and computer-aided tools ultimately determine the quality of the software [52].

- *Data dictionary:* The software application does not have a data dictionary. Though, implicitly through C library documentation from the proprietary devices, each of the drivers developed have loose data dictionaries.

- *Uniformity:* The software design practices strict uniformity with data structures. For example, a requirements attribute is implemented on every *Procedure* and *Device* parent class, enforcing various elements and related information to exist within each of the child classes.

- *Prototyping:* The software design fully supports prototyping with the user's ability to interact with the additive system through communication directly to the *Device* child classes. In fact, this practice is encouraged in order to give the user the ability to venture with functions to best equip their experiment.

- *User involvement:* User involvement was minimal during the software development.

- *Documentation:* The software is documented with primitive coding comments. Not all functions and classes are properly commented and the format is not standard. No additional documentation outside of coding comments exists.

- *Computer-aided tools:* The software application is purely command-line and script dependent. However, the software design is ready for Graphical User Interface (GUI) implementation. This feature is out of scope for this study and available for future work.

4.2 Experimental Design and Data Collection Review

The design of the experiment and quality of the data are crucial for the fruition of the height estimation algorithm. There are several successes and shortcomings of the design of experiment that affected the quality of the data collected. Overall, the experiment designed for data collection was advantageous given some constraints and limitations.

Constraints and Limitations.

The most prominent limitation of the experiment is the fixed central camera position constraint. The additive system currently only supports a single camera mounted parallel to the z-axis. Through iterative testing of the experimental design and photometric stereo results, creation of a multi-positioned mount is considered to support stereo vision techniques. This option is averted as a result of the inability to assure precise camera placement between execution of trials.

The experiment needed to be repeatable and reliable to assure consistency and reliability in the quality of the data and ultimately the height estimation algorithm. In order to assure this high level of precision and consistency between trials, the additive system required a professional mechanical mount to control the camera's position, which was not available at the time of this study. The implications of this constraint is that it limited the capability of the system solely to the collection of imagery from a fixed position. Not only this, but the viewing direction is perpendicular to the image plane, which requires the use of solely shading cues to estimate depth. Thus, the study could not test various surface reconstruction and depth estimation techniques to compare to the photometric stereo method.

Another significant limitation of the experimental design is the lack of a method for gathering true depth measurements. Without this ability, this study lacks the ability to evaluate the accuracy of the depth maps produced from the photometric stereo method. One method to mitigate this limitation would be use range imaging in tangent to monocular imaging similar to the works of Mou and Zhu [53].

Shortcomings.

The experimental design mass produced extrusions with little human intervention. The only required labor per a trial is to move the light source position since the

light source mount has fixed positions. As a result of mass production with little moderation, many trials produced sample failures. Figure 21 shows a few examples
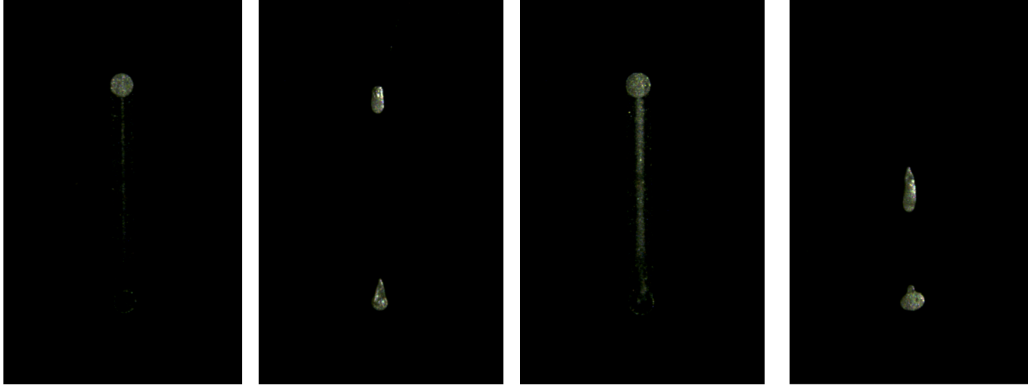
Figure 21. Failed samples due to extrusion abnormalities.

of sample failures. In attempt to prevent these failed cases, the nozzle cleansing well was added to the print automation. At the expense of an extended trial completion duration, the well helps maintain the Silver Poly(Methyl Methacrylate) (Ag-PMMA) viscosity to promote constant extrusion rate.

Successes.

Despite the limitations and shortcomings, the final iteration of the experimental design provided an almost fully automated mass production of sample extrusions. With the addition of an automated light source placement capability, as well as an adequate height estimation mechanism, the experiment would be able to fully automate the data collection and maintain the quality of the printed samples.

4.3 Data Preprocessing Review

Image Processing.

The image preprocessing is prosperous for extrusions without abnormalities. However, it is not absolutely robust, which resulted in its failure in many cases. Many samples of imperfect extrusions were lost due to the strict bounds set by the image processing input parameters. Figure 22 depicts the image processing sequence for an extrusion with abnormal structural integrity. In this example, the nozzle experienced
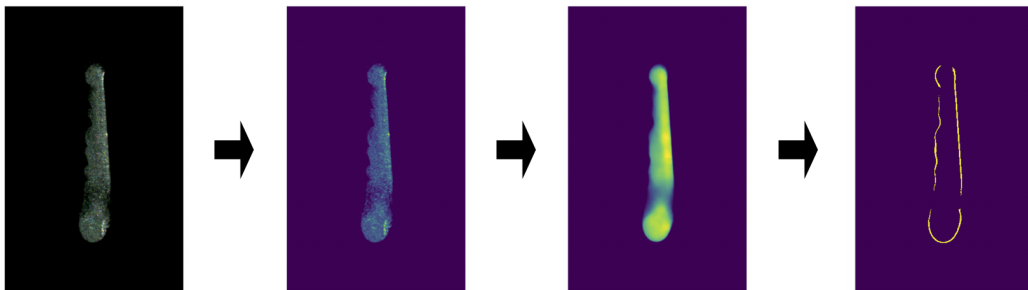
Figure 22. Image processing failure on an abnormal extrusion.

interference, likely due to particle build up, and the extrusion rate was not consistent across the sample. Thus, the exterior is coarse and the result of the image processing sequence returns an invalid mask, rendering an otherwise serviceable sample useless. The fix to this issue does not rely on simple tweaks to the filters and threshold input parameters, as the values chosen for the input parameters are most consistent with the majority of the sample population. Regulating this issue would require intelligent detection of the overall image intensity and correction of coarse print boundaries in order to ensure a closed max after filters and thresholds are applied.

Height Extraction.

The height extraction technique is straightforward, as it simply derives height measurements from a saved JavaScript Object Notation (JSON) file. It must be noted that the validity of the height measurements are questionable as result of the automation of a mass number of samples per data collection trial. Recall Figure 19. Many height measurements are near zero. For samples closest to the x- and y axes, these measurements are logical due to the near zero tip height print parameters. However, the pattern of near zero measurements remain throughout the entire print, which suggests that some touch probe measurements may have missed contact with the printed extrusion. This circumstance is probable considering the automation technique used to gather height measurements in rapid succession. Additionally, the samples' area of extrusion are not consistent across each sample.

As previously mentioned, the height measurements are calculated at the lowest point of the probe imprint. This marginal error in true height to measured height ultimately affects the accuracy of the height estimation algorithm, which is not represented by model testing. Thus, even if the height estimation model perfectly estimated the measured heights from the depth calculations, an unknown marginal error still exists.

4.4 Photometric Stereo and Depth Estimation Review

The following sections evaluate the photometric stereo method used for surface reconstruction as well as the depth estimation method used to create data for the height estimation model.

Photometric Stereo.

The photometric stereo method was successful at extracting each sample's surface orientation by calculating the normal vectors for each coordinate of a sample set of images. We can assess the quality of the surface normal calculations by observing a map of the surface normals. Using the same sample extrusion images shown in Figure 16, Figure 23 displays a map of the surface normals using Red, Green, and Blue (RGB) encoding as well as a plot of the surface normal values across the width of the sample.
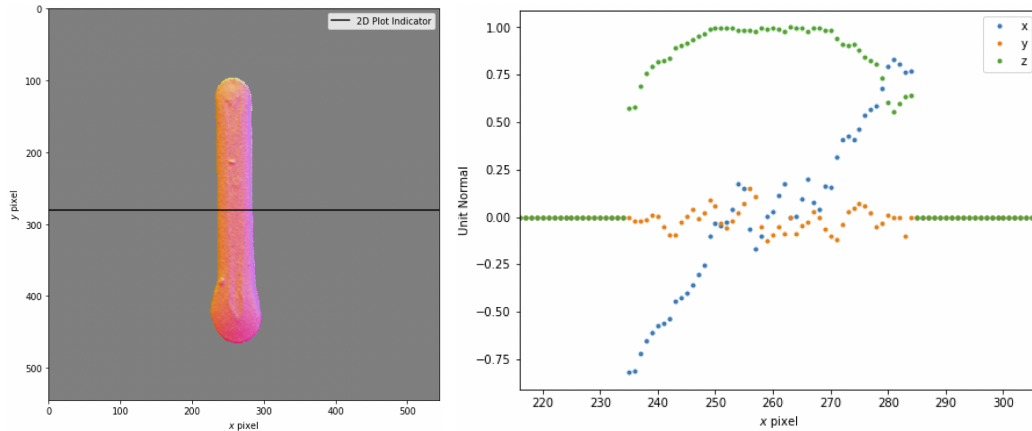
Figure 23. A normal map representing a sample's surface orientation (left) and a 2D visual of the normals across the width of the sample (right).

Even though the normal map is a 2D image, it is capable of depicting the 3D array of surface normal values calculated from the photometric stereo method. The RGB color channels in the map correspond to the respective z, y, and x unit vector values of the surface normals at each pixel coordinate. The normal map color encoding is compatible with the structural formation of the extrusion. There is no representation of color for the green channel. This is coherent because of the orientation of the viewing plane being directly parallel to the image plane; rather, the images were

49

taken with the camera perpendicular to the printing substrate. The z vector values are also consistent with the line's structure; at the upper tip of the extrusion the yellow color indicates the northern falloff and at the lower tip of the extrusion the red color indicates the southern falloff. Finally, the pink color on the right side of the extrusion is a result of the strong blue encoding—a positive x normal unit vector—mixing with the red encoding of the z. The left side of the extrusion does not experience color encoding in the x-direction, as the unit normals are negative values. This representation accurately depicts the arch shape of the extrusion across its width. The scatter plot in Figure 23 is a two-dimensional representation of this same color encoding pattern previously described for a single row of the normal unit vector values, which is indicated by the black line on the normal map.

Depth Estimation.

The depth estimation method was successful at deriving each sample's relative distance from the viewing plane by using the normal unit vectors to calculate the depth from neighboring pixels at each coordinate across the array of surface normals. Despite the efforts of using spare matrices, the iterative process of comparing both vertically and horizontally neighboring pixels (Equation 15) is highly computationally demanding, which warrants the need to downsample the original images to half their captured resolution. Computing the depth maps on the original image resolutions resulted in runtimes greater than ten minutes per sample. However, these results were obtained on the computing system used to create the height estimation algorithm, which has significantly greater processing power than the MEAM printer's computing system. Thus, in order to promote a practical solution for online height estimation, the original images are downsampled. Downsampling the images to half their original resolution reduces the runtime of the depth estimation algorithm to approximately

50

15 seconds per sample on the development computing system.

In the same manner as with the surface normals, we can evaluate the worth of the calculated depths by observing the depth map. Again, using the same sample, Figure 24 displays both a two-dimensional and three-dimensional view of the estimated relative depths from the viewing plane, as well as one of the original images for reference.
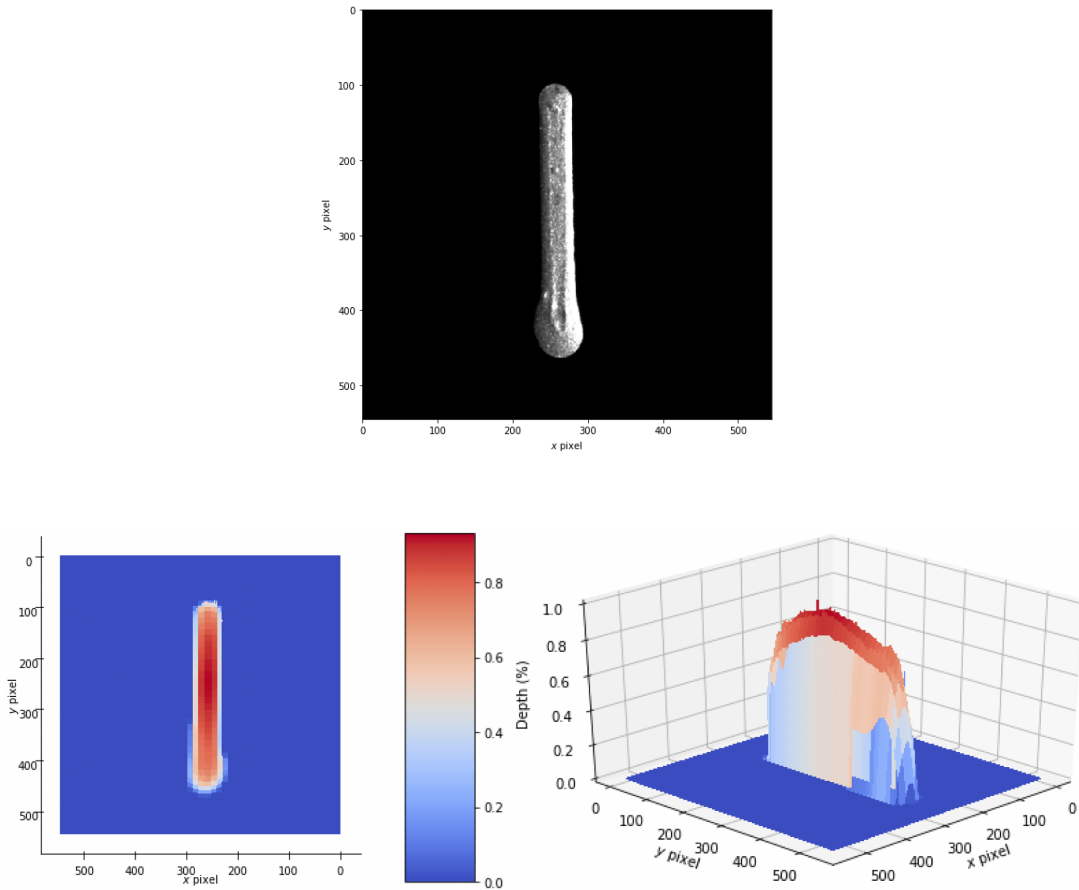
Figure 24. A sample extrusion (top) and depth maps representing its estimated depth in both 2D (bottom left) and 3D (bottom right) representations.

The depth map shows a relatively accurate depiction of the surface architecture of the sample extrusion. It lacks detail in the definition of its curvature, which is best portrayed by the lack of a cavity in the lower region. Additionally, the depth map

displays minute noise, exhibited by the spikes in the 3D representation. Despite these deficiencies, the algorithm does attempt to recognize depth variation across the length of the line. The original image shows a larger mass of extrusion at the start of the print ($y \approx 450$) than at the finish of the print ($y \approx 100$), giving visual cue of a decrease in height in the same direction. Figure 25 best shows this with its two-dimensional plots of depth values along both the length and width of the extrusion.
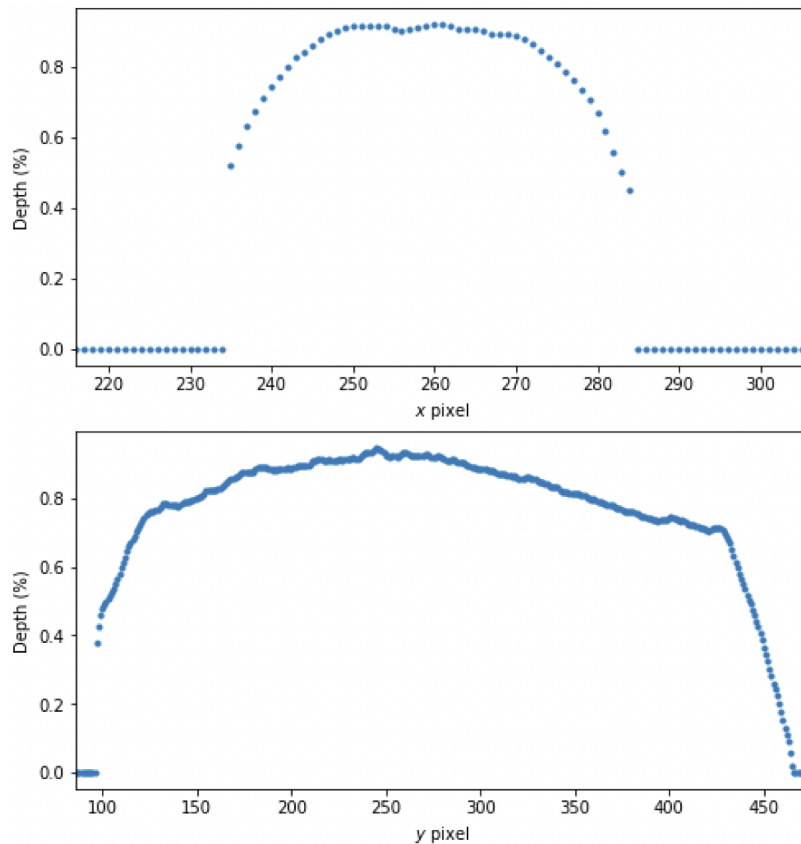
Figure 25. 2D visuals of the estimated depths across the width (top) and the length (bottom) of the sample.

In addition, Figure 25 also shows why the areas for computing the average depth in a region, as discussed in Section 3.4, were reduced. As expected, the depths at each end of both the 2D length and width plots show drastic falloff. Figure 26 shows the contour plot of the extrusion's estimated depth split by regions.
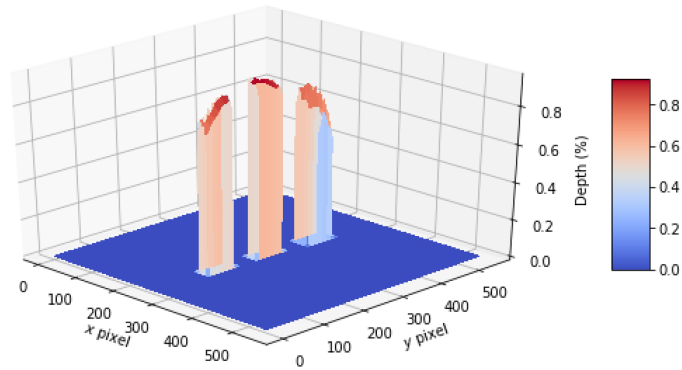
Figure 26. A sample's 3D visual of depth by region.

Again, the effect of the average depth calculated is better seen with the two-dimensional plots of the depth by length and width. Figure 27 shows the depths by length and width with indications of region boundaries. The depths in the shaded regions of interest are selected for regional depth values.
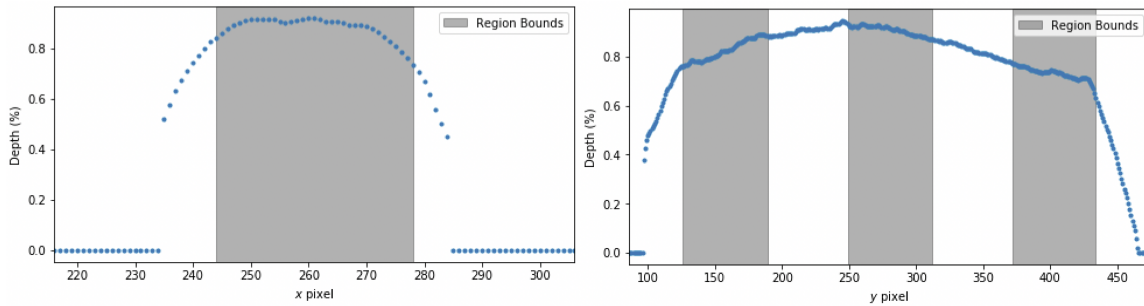
Figure 27. 2D visuals of the estimated depths across the width (left) and the length (right) of the sample with region indicators.

This technique is a robust method for producing three accurate values for the relative depth of each sample. Despite this, the computed relative depth values do not adequately represent the measured height values. For example, this sample's height measurements are $48.93\,\mu$m, $35.23\,\mu$m, and $9.05\,\mu$m, but its respective depth values are 0.82%, 0.90%, and 0.72%. Though this example does follow an appropriate

decreasing order, the slope of descent between the second and third measurements do not correlate. This sample is showcased because this occurrence is most common amongst the sample population. However, there are many samples that do not sustain the decreasing order but rather have mismatching slopes of change between height measurement and estimated depth. Thus, this adversely affects the capacity of the height estimation algorithm, as the predictive model will unfavorably predict heights on skewed data.

Additional Considerations.

In addition to the negative impacts discussed in the previous section, the height estimation algorithm is negatively affected by the fact that the depth estimates are relative percentages calculated on a per sample basis. The depth estimation algorithm does not consider the depths of the population. The implications of this are that the weights of the depth values are significantly dishonest as extrusions of smaller mass will receive similar relative depths to extrusions of larger mass. Thus, the estimated depths do not drastically differ between samples printed at lower tip height settings from samples printed at higher tip height settings. Again, this adversely impacts the capacity of the predictive model discussed in the next section because it is not able to accurately discern between samples of different dimensions.

4.5   Predictive Model Review

The following section reviews the process for creating the height prediction model. First, various statistical tools allow the analysis of the input data. Using a training and validation sample set, along with various analytical methods, the model is selected for the height estimation algorithm. Finally, we review the performance of the model on the test dataset.

Data Visualization.

The input data into the regression model is comparably simple as there is only a single parameter, the estimated depths. Recall the dataset is reduced to one-third its size by extracting only the middle depth values. This leaves the data population to 187 samples with a single relationship between each sample: depth and height. Figure 28 shows the data distributions for each of the split regions.
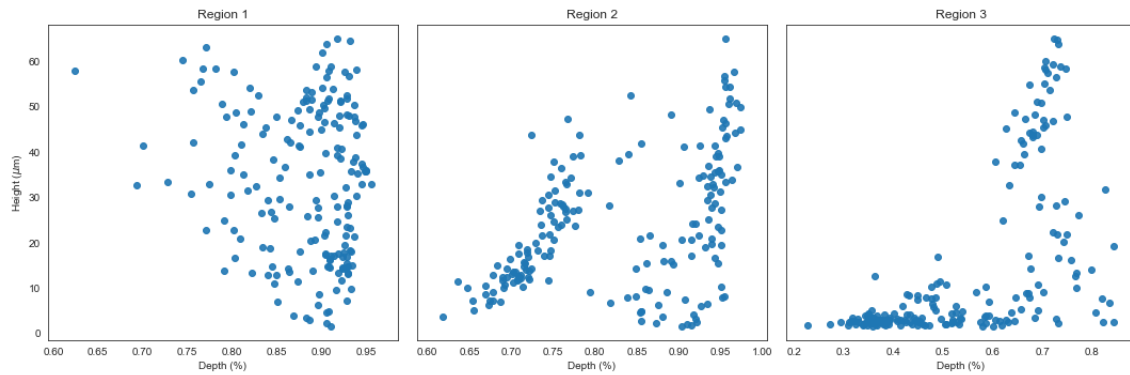
Figure 28. Scatter plots showing the data distribution for each average depth plotted against its measured height.

Region 3 has the highest Pearson correlation coefficient of 0.61, which shows that it has the strongest linear relationship. Though this would suggest Region 3 as the best option for model height prediction, the correlation is artificial as a result of the numerous near-zero height measurements. Region 1's correlation is -0.15, meaning it does not have a linear relationship, and consequently its relationship to depth is unintelligible. Thus, the only sensible region to use for the height estimation model is Region 2, despite its weak correlation to depth with a coefficient of 0.44. Figure 29 shows another look at the data distribution for Region 2. The depth histogram is inconsistent with the height histogram, which shows large imbalance and reinforces the conclusion of weak linear correlation. Nonetheless, we attempt to fit a nonlinear model to the data using multiple linear regression.
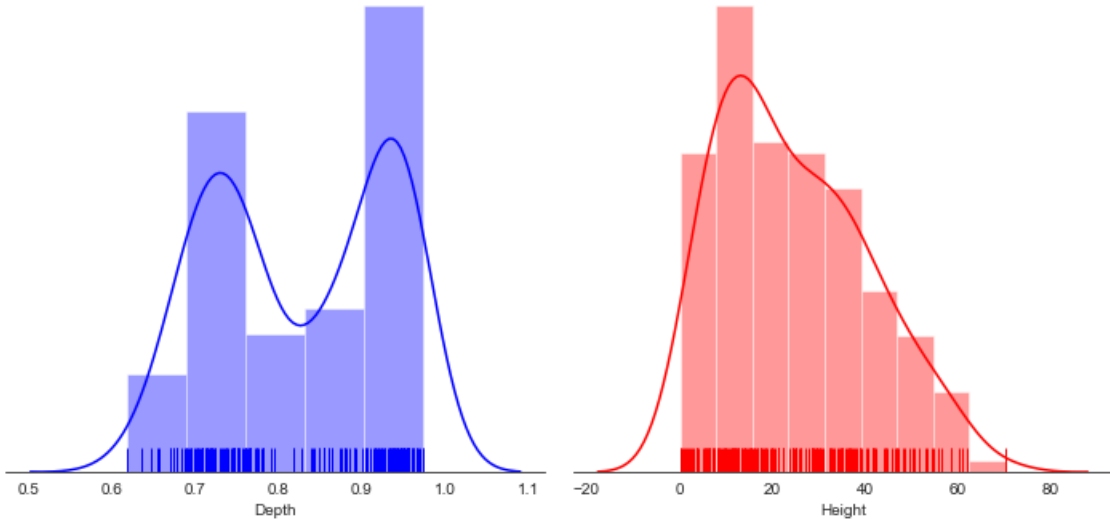
Figure 29. Distribution histograms of Region 2 depths and heights.

Model Selection.

In order to utilize multiple linear regression, artificial parameters are created by generating a new feature matrix consisting of all the polynomial combinations of the depth parameter with a degree up to 8. Thus, the number of input parameters to each model depends on which polynomial is tested. The depth values then follow Equation 16.

$$X \ni \begin{cases} Depth \\ Depth + Depth^2 \\ Depth + Depth^2 + Depth^3 \\ \quad \vdots \qquad\quad \vdots \qquad\quad \vdots \\ Depth + Depth^2 + \quad ... \quad + Depth^8 \end{cases} \tag{16}$$

Using the training and validation set, each of the eight models are evaluated using the Mean Squared Error (MSE) as the performance measurement. The MSE statistic is favorable, as it explains how close the fitted regression line for each model is to the prediction data points. It does this by calculating the error distances from each point to the regression line and then squares this value to penalize greater errors more heavily. Figure 30 displays the results of testing each model across 50 different training and validation set variations using random seeds to control the composition of each sample set.
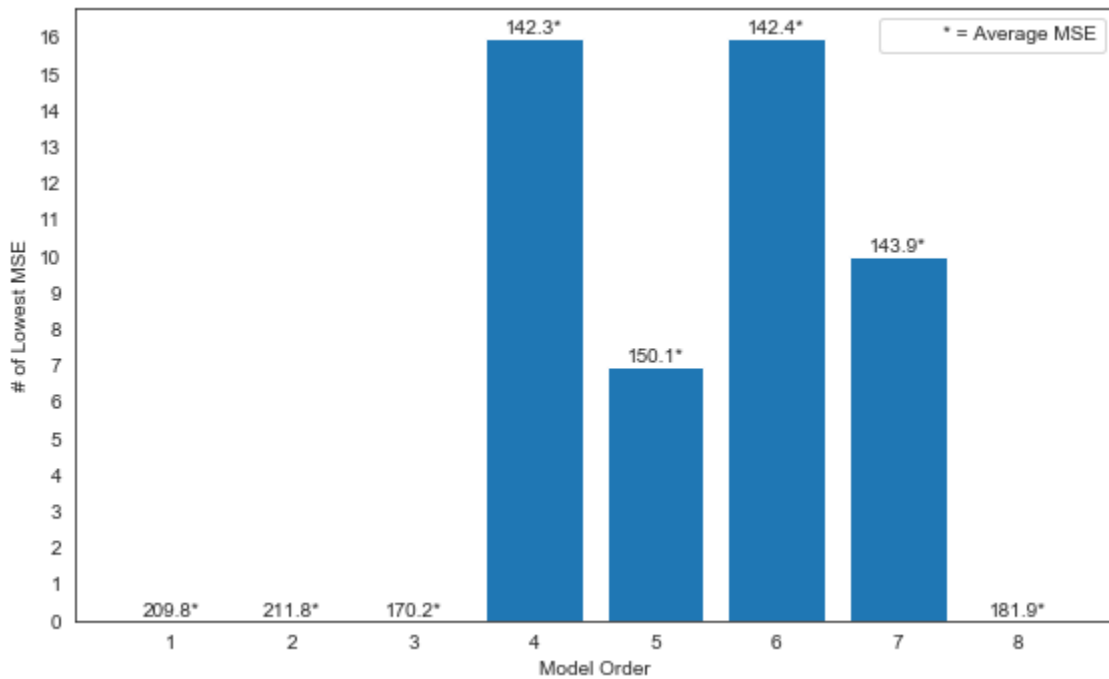
Figure 30. **Metric comparison of the performance of the models tested via cross-validation.**

Over the 5-fold cross-validation method, the quadratic and sextic models tied for having the lowest scoring MSE at 16 random seeds each. The average MSE across each polynomial model are almost identical. The quadratic model is chosen not only because it slightly outperforms the sextic model, but having a lower polynomial

order model encourages generalizing the model by preventing the heavy overfitting of the model on the training data. The average MSE values across all models are extraordinarily high, which indicates that all of the models tested are performing relatively unsatisfactory on all variations of the training set.

Model Testing.

Using the entire nontest dataset (combination of both training and validation sets), the final model is trained using the quadratic polynomial order to make predictions on the test dataset. Figure 31 provides a complete summary of the performance of the final model including relevant statistical measures.

```
                          OLS Regression Results
====================================================================================
Dep. Variable:                      y    R-squared:                       0.516
Model:                            OLS    Adj. R-squared:                  0.502
Method:                 Least Squares    F-statistic:                     38.33
Date:                Mon, 18 Feb 2019    Prob (F-statistic):           8.18e-22
Time:                        23:25:13    Log-Likelihood:                -571.38
No. Observations:                 149    AIC:                             1153.
Df Residuals:                     144    BIC:                             1168.
Df Model:                           4
Covariance Type:            nonrobust
====================================================================================
                 coef     std err          t      P>|t|      [0.025      0.975]
------------------------------------------------------------------------------------
const         2.805e+04   5681.780      4.936      0.000    1.68e+04    3.93e+04
x1           -1.491e+05   2.88e+04     -5.184      0.000   -2.06e+05   -9.22e+04
x2            2.944e+05   5.42e+04      5.428      0.000    1.87e+05    4.02e+05
x3           -2.56e+05    4.52e+04     -5.663      0.000   -3.45e+05   -1.67e+05
x4            8.276e+04   1.4e+04       5.892      0.000    5.5e+04     1.11e+05
====================================================================================
Omnibus:                        2.730    Durbin-Watson:                   2.116
Prob(Omnibus):                  0.255    Jarque-Bera (JB):                2.507
Skew:                           0.138    Prob(JB):                        0.285
Kurtosis:                       3.573    Cond. No.                     1.41e+05
====================================================================================
```

Figure 31. **Summary of statistical measures on the final prediction model.**

This ordinary least squares regression report provides an abundance of information on the salience of the height predictive model. The R^2 and Adjusted-R^2 are measures of overall performance of the model, and suggest the model explains approximately 50% of the variation in the depth estimations. The Adjusted-R^2 value being marginally lower than the multiple R^2 suggests the additional polynomial terms do not adversely affect the model. We can confirm this with the p-values (P > |t|) all being under

0.05, which statistically supports their relevance. Hence, the coefficients for each dependent variable are not near zero and we can reject the null hypothesis. Finally, the conditional number is large at 1.41e+05, which suggests strong multicollinearity between the dependent variables. This is logical, as the dependent variables are artificially conceived from a single dependent variable. Many of the other statistics shown are measures of residual spatial autocorrelation (ensuring residuals are spatially random), model stationarity (model's consistent relationship to the dependent variables), model bias (whether residuals are normally distributed), and model significance (overall statistical significance). Figure 32 shows a plot of the residual errors for each prediction on the test dataset.
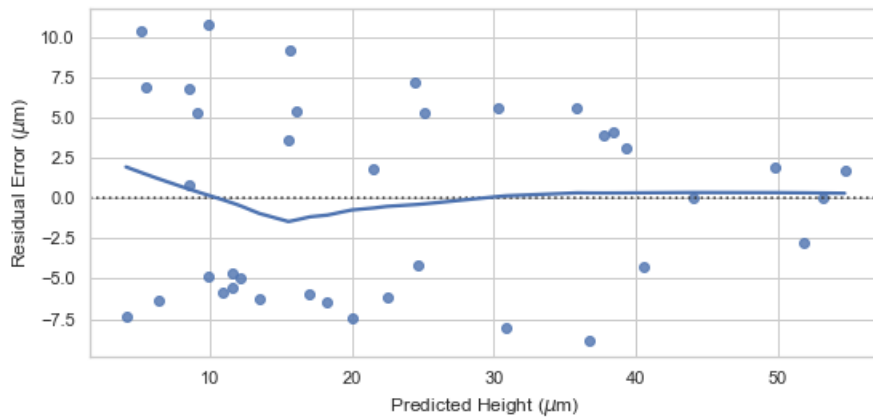
Figure 32. Plot of the residual errors on the test data.

From the residual plot, we can see that the model has low bias but high variance. This is seen with the near-zero average residual error but large residual error disparity. Thus, the model is predicting heights consistently but inaccurately. Additionally, the residual plot shows a larger prediction error for smaller measured samples than larger measured samples. This trend is consistent with the relative depth estimation limitation. Because depths are calculated relative to each sample, the smaller measured

samples are penalized more by higher depth estimations.

4.6 Summary

This chapter reviewed the methods used to create a height estimation algorithm for monocular imagery. Given the limitations involved with these methods, each of the software, experimental, and algorithmic designs have successes and failures that influence the final height estimation tool. The prediction model is analyzed using strong statistical techniques and assess for on its overall relevance. The final height estimation method has a strong algorithmic process and but shows lackluster performance on test data.

V. Conclusion

Additive systems provide many benefits over traditional technologies for the manufacturing of metallic products by lending a cost-effective and environment-friendly engine for the quick customization of unique parts. The technology's cutting-edge innovation has spearheaded an outbreak of research across many of the additive manufacturing processes. However, there remains a need for automation and process control of Material Extrusion Additive Manufacturing (MEAM) systems in order to increase the overall level of quality assurance in industrialized printing. The primary goal of this study was to provide a non-contact height estimation mechanism for Air Force Research Laboratory (AFRL)/Materials and Manufacturing Directorate, Functional Materials Division, Soft Matter Materials Branch (RXAS) in order to increase their MEAM system's product quality assurance.

In attempt to create a height estimation mechanism for AFRL/RXAS, a software system, depth estimation algorithm, and multiple linear regression model were created. The software system is a fully functional, hardware robust design; it is designed to support automation and process control of the additive system. Due to hardware constraints, the height estimation algorithm is limited to the use of the photometric stereo method for surface reconstruction and depth estimation. Using a fixed camera position confines the algorithm to calculating relative depth for each sample. This implication along with the mass production of extrusions through an iteration of experimental design negatively affects the quality of the data collection. Consequently, the predictive model constructed in this study is unable to produce height estimations with the level of accuracy demanded by the MEAM system.

5.1 Research Conclusions

Despite the under-performing predictive model, this research contributes in exploration of process control for quality assurance in MEAM systems. This study draws the following conclusions:

- The design of a process monitoring tool for height estimation via imagery requires absolute depth calculations. Photometric stereo surface reconstruction is an inadequate technique for this endeavor as it provides relative depth. Techniques such as stereo vision or range imaging are better suited for the problem of height estimation in additive systems.

- Viewing angles perpendicular to the printing substrate are not sufficient for height estimation from monocular imagery because they constrain the gathering of depth information to shading cues. Viewing angles with appropriate angles of tilt provide relative distance cues and empower vergence, object placement relation, and familiar size depth estimation techniques. Additionally, tilted viewing angles provide information on the detail of both the top and sides of extrusions.

- Mass production of samples jeopardize the quality of extrusions. Though this method may be unavoidable for a number of machine learning research applications in the MEAM field, real-time collection of data is credibly more appropriate than its in-situ counterparts. High availability of powerful computing systems in today's industry lends the proposition for use of video systems over still images.

- Furthermore, the prevalence of the Convolutional Neural Network (CNN) in modern research along with their profound results on computer vision tasks

warrants the use of deep learning techniques over the classic depth perception techniques discussed in Chapter II.

5.2 Future Work

As a system whose success is substantially dependent on the transient, physical effects of both the printing environment and extrusion material(s) properties, in addition to the technology-specific limitations of the system, the printing process and signature parameter space for production optimization is extremely large. Thus, the opportunities for optimization of additive systems are truly limitless. Below are few research opportunities closely related to the aim for non-contact height estimation in MEAM.

- The most immediate work to follow is the design of an adequate predictive algorithm for height estimation. Whether it be stereo vision or ranging imaging, relative distance cues or CNNs, the first step to quality assurance is height estimation of single extrusion layer. The ability to measure a single extrusion layer without contact with a high confidence interval is paramount for the growth of MEAM. Only then can the process parameter and signature space expand to more complex structures and materials.

- Though there are several viable avenues to pursue for a height estimation algorithm, the work of Iravani-Tabrizipour and Toyserkani is promising for the application of MEAM. Utilizing three Charge-Coupled Device (CCD) cameras with interference filters and lenses, their algorithm which combines an image-based tracking protocol and a recurrent neural network to extract the clad height in real-time is able to detect the clad height independent from clad paths in the laser cladding process with about 12% maximum error [45]. Exploiting a

trinocular optical system with tilted viewing angles empowers a height estimation algorithm with strong depth cues encompassing the entirety of a printed structure for an accurate stereo vision implementation. Though the authors employ an Elman Recurrent Neural Network (RNN) to detect any dynamic disturbances in the network inputs generated by noise in the images, other feature extraction algorithms, such as a CNN, are equally viable approaches.

- Once the height estimation algorithm has a high confidence interval feasible for production, it can be integrated into the computing system to enable a closed-loop control system. The premise behind how this is accomplished is that the height estimator will calculate a height from a given image—or set of images. This value is then compared to the target height defined in the software apparatus's toolpath generation. For single-layer print correction, the estimated height will be used to adjust the print parameter settings depending on if the calculated height is greater than or less than the target height. The single-layer must then be reprinted using the adjusted settings. For multi-layer print correction, subsequent layer print parameter settings are adjusted in a likewise manner. However, multi-layer print correction can adjust at runtime to allow real-time correction of the print.

5.3 Final Remarks

As automation and process control become more pervasive in MEAM, so too will the additive manufacturing process in common industry. Despite the lessons learned, this study equipped AFRL/RXAS with a software solution capable of integrating process monitoring tools for the automation of print correction. This product readies the United States Air Force with the capacity to adapt with the evolution of additive systems and rapid prototyping.

Bibliography

1. ASTM International, "F2792-12a - Standard Terminology for Additive Manufacturing Technologies," *Rapid Manufacturing Association*, pp. 10–12, 2013. [Online]. Available: http://www.ciri.org.nz/nzrma/technologies.html

2. I. Gibson, D. Rosen, and B. Stucker, *Additive Manufacturing Technologies*, 2nd ed. New York: Springer Science+Business Media, 2015.

3. S. Huang, P. Liu, A. Mokasdar, and L. Hou, "Additive manufacturing and its societal impact: A literature review," *International Journal of Advanced Manufacturing Technology*, vol. 67, pp. 1191–1203, 2012.

4. D. Thomas and S. Gilbert, "Costs and Cost Effectiveness of Additive Manufacturing: A Literature Review and Discussion," National Institute of Standards and Technology, U.S. Department of Commerce, Tech. Rep., 2014. [Online]. Available: https://www.uni-due.de/~adf040p/talks/BasicMRI.pdf

5. D. P. Tabor, L. M. Roch, S. K. Saikin, C. Kreisbeck, D. Sheberla, J. H. Montoya, S. Dwaraknath, M. Aykol, C. Ortiz, H. Tribukait, C. Amador-Bedolla, C. J. Brabec, B. Maruyama, K. A. Persson, and A. Aspuru-Guzik, "Accelerating the discovery of materials for clean energy in the era of smart automation," *Nature Reviews Materials*, vol. 3, no. 5, pp. 5–20, 2018.

6. M. Mani, B. M. Lane, M. A. Donmez, S. C. Feng, and S. P. Moylan, "A review on measurement science needs for real-time control of additive manufacturing metal powder bed fusion processes," *International Journal of Production Research*, 2016.

7. K. Kyrgyzova, "Uncalibrated non-Lambertian photometric stereo," Ph.D. dissertation, 2014. [Online]. Available: http://pages.cs.wisc.edu/~lizhang/courses/cs766-2008f/syllabus/10-09-shading/shading.pdf

8. D. P. Curtin, "Digital photography," in *The Textbook of Digital Photography*, 2nd ed., 2007, ch. Chapter 1:, pp. 9–41. [Online]. Available: http://www.shortcourses.com

9. J. Butime, L. G. Corzo, and C. F. Espronceda, "3D Reconstruction Methods, a Survey," *Proceedings of the First International Conference on Computer Vision Theory and Applications*, pp. 457–463, 2006. [Online]. Available: http://www.scitepress.org/DigitalLibrary/Link.aspx?doi=10.5220/0001369704570463

10. S. M. Seitz, "An Overview of Passive Vision Techniques," *Proc. of SIGGRAPH*, pp. 1–3, 1999.

11. E. Prados and O. Faugeras, "Shape From Shading," in *Handbook of Mathematical Models in Computer Vision*, N. Paragios, Y. Chen, and O. Faugeras, Eds. Springer, 2006, ch. 23, pp. 375–388.

12. P. Belhumeur, D. Kriegman, and A. Yuille, "The Bas-Relief Ambiguity," *International Journal of Computer Vision*, pp. 1060–1066, 1997.

13. R. Klette, R. Kozera, and K. Schluns, "Shape from Shading and Photometric Stereo Methods," Computer Science Department of The University of Auckland CITR at Tamaki Campus, Tech. Rep., 1998.

14. R. Jain, R. Kasturi, and B. G. Schunck, "Shading," in *Machine Vision*, 1995, pp. 257–275.

15. M. Khanian, A. S. Boroujerdi, and M. Breuß, "Photometric stereo for strong specular highlights," *Computational Visual Media*, 2017.

16. M. H. Weik, "Lambert's cosine law," in *Computer Science and Communications Dictionary*. Boston, MA: Springer US, 2001, p. 868. [Online]. Available: https://doi.org/10.1007/1-4020-0613-6_9901

17. S. Nayar, R. Ramamoorthi, and P. Hanrahan, "Basic Principles of Surface Reflectance." [Online]. Available: https://www.cs.cmu.edu/afs/cs/academic/class/15462-f09/www/lec/lec8.pdf

18. R. Zhang, P.-s. Tsai, J. E. Cryer, and M. Shah, "Shape from Shading : A Survey," *Review Literature And Arts Of The Americas*, vol. 21, no. 8, pp. 690–706, 1999. [Online]. Available: http://ieeexplore.ieee.org/xpls/abs_all.jsp?arnumber=784284

19. J. Ackermann and M. Goesele, "A Survey of Photometric Stereo Techniques," *Found. Trends. Comput. Graph. Vis.*, vol. 9, no. 3-4, pp. 149–254, 11 2015. [Online]. Available: http://dx.doi.org/10.1561/0600000065

20. L. Zhang, "Photometric Stereo," 2008.

21. R. J. Woodham, "Photometric Method For Determining Surface Orientation From Multiple Images," *Optical Engineering*, vol. 19, no. 1, pp. 139–144, 1980. [Online]. Available: http://opticalengineering.spiedigitallibrary.org/article.aspx?doi=10.1117/12.7972479

22. K. Ikeuchi, "Determining Surface Orientations of Specular Surfaces by Using the Photometric Stereo Method," *IEEE Transactions on Pattern Analysis and Machine Intelligence*, vol. PAMI-3, no. 6, pp. 661–669, 1981.

23. G. Kay and T. Caelli, "Estimating the Parameters of an Illumination Model," pp. 365–388, 1995.

24. A. Georghiades, "Incorporating the Torrance and Sparrow Model of Reflectance in Uncalibrated Photometric Stereo," *Proceedings of the Ninth IEEE International Conference on Computer Vision*, 2003. [Online]. Available: http://ieeexplore.ieee.org/document/1238432/

25. L. Shen, T. Machida, and H. Takemura, "Efficient Photometric Stereo Technique for Three-Dimensional Surfaces with Unknown BRDF," *Proceedings of the Fifth International Conference on 3-D Digital Imaging and Modeling*, pp. 326–333, 2005.

26. H. S. Chung and J. Jia, "Efficient Photometric Stereo on Glossy Surfaces with Wide Specular Lobes," *26th IEEE Conference on Computer Vision and Pattern Recognition, CVPR*, 2008.

27. J. F. Blinn, "Models of Light Reflection for Computer Synthesized Pictures," *ACM SIGGRAPH Computer Graphics*, vol. 11, no. 2, pp. 192–198, 1977. [Online]. Available: http://portal.acm.org/citation.cfm?doid=965141.563893

28. B. T. Phong, "Illumination for Computer Generated Pictures," *Communications of the ACM*, vol. 18, no. 6, 1975.

29. P. R. Sanz, B. R. Mezcua, and J. M. Sánchez Pena, "Depth Estimation-An Introduction," 2012. [Online]. Available: http://dx.doi.org/10.5772/45904

30. D. Mohan and A. R. Ram, "A review on depth estimation for computer vision applications," *International Journal of Engineering and Innovative Technology*, vol. 4, no. 11, pp. 235–239, 2015.

31. T. Koch, L. Liebel, F. Fraundorfer, and M. Körner, "Evaluation of CNN-based Single-Image Depth Estimation Methods," pp. 1–21, 2018. [Online]. Available: http://arxiv.org/abs/1805.01328

32. A. K. Macworth, "Interpreting Pictures of Polyhedral Scenes," *Artificial Intelligence*, vol. 4, no. 2, pp. 121–137, 1973.

33. K. Ikeuchi and B. Horn, "Numerical Shape from Shading and Occluding Boundaries," *Artificial Intelligence*, pp. 141–184, 1980.

34. S. Shafer, K. Takeo, and J. Kender, "Gradient Space Under Orthography and Perspective," Ph.D. dissertation, Carnegie-Mellon University, 1982.

35. K. Ikeuchi, "Constructing a Depth Map from Images," Massachusetts Institute of Technology, Artificial Intelligence Laboratory, Arlington, Tech. Rep., 1983.

36. G. Tapia and A. Elwany, "A Review on Process Monitoring and Control in Metal-Based Additive Manufacturing," *Journal of Manufacturing Science and Engineering*, vol. 136, 2014. [Online]. Available: http://manufacturingscience. asmedigitalcollection.asme.org/article.aspx?doi=10.1115/1.4028540

37. I. D. S. Melvin, L. S. and J. Beaman, S., "Video Microscopy of Selective Laser Sintering," *Proceedings of the Solid Freeform Fabrication Symposium*, pp. 34–41, 1994.

38. S. Berumen, F. Bechmann, S. Lindner, J. P. Kruth, and T. Craeghs, "Quality control of laser- and powder bed-based Additive Manufacturing (AM) technologies," *Physics Procedia*, vol. 5, no. PART 2, pp. 617–622, 2010.

39. S. Kleszczynski, J. z. Jacobsmühlen, J. T. Sehrt, and G. Witt, "Error Detection in Laser Beam Melting Systems," *FFF Workshop*, pp. 975–987, 2012.

40. J. P. Kruth and P. Mercelis, "Procedure and Apparatus for In-Situ Monitoring and Feedback Control of Selective Laser Powder Processing," 2009.

41. W. Serruys, J. D. Keuster, J. Duflou, and J. P. Kruth, "Arrangement and Method for the Online Monitoring of the Quality of a Laser Process Exerted on a Workpiece," 2011.

42. T. Craeghs, F. Bechmann, S. Berumen, and J. P. Kruth, "Feedback control of Layerwise Laser Melting using optical sensors," *Physics Procedia*, vol. 5, no. PART 2, pp. 505–514, 2010. [Online]. Available: http://dx.doi.org/10.1016/j.phpro.2010.08.078

43. T. Craeghs, S. Clijsters, E. Yasa, F. Bechmann, S. Berumen, and J. P. Kruth, "Determination of geometrical factors in Layerwise Laser Melting using optical process monitoring," *Optics and Lasers in Engineering*, vol. 49, no. 12, pp. 1440–1446, 2011. [Online]. Available: http://dx.doi.org/10.1016/j.optlaseng.2011.06.016

44. T. Craeghs, S. Clijsters, J. P. Kruth, F. Bechmann, and M. C. Ebert, "Detection of Process Failures in Layerwise Laser Melting with Optical Process Monitoring," *Physics Procedia*, vol. 39, no. December, pp. 753–759, 2012.

45. M. Iravani-Tabrizipour and E. Toyserkani, "An image-based feature tracking algorithm for real-time measurement of clad height," *Machine Vision and Applications*, vol. 18, no. 6, pp. 343–354, 2007.

46. L. Song, V. Bagavath-Singh, B. Dutta, and J. Mazumder, "Control of melt pool temperature and deposition height during direct metal deposition process," *International Journal of Advanced Manufacturing Technology*, vol. 58, no. 1-4, pp. 247–256, 2012.

47. A. Fathi, A. Khajepour, M. Durali, and E. Toyserkani, "Geometry Control of the Deposited Layer in a Nonplanar Laser Cladding Process Using a Variable Structure Controller," *Journal of Manufacturing Science and Engineering*, vol. 130, no. 3, p. 031003, 2008. [Online]. Available: http://manufacturingscience.asmedigitalcollection.asme.org/article.aspx?articleid=1452040

48. E. Toyserkani and A. Khajepour, "A mechatronics approach to laser powder deposition process," *Mechatronics*, vol. 16, no. 10, pp. 631–641, 2006.

49. E. Toyserkani, A. Khajepour, and S. Corbbin, "System and Method for Closed-Loop Control of Laser Cladding By Powder Injection," 2006.

50. P. Nikolaev, D. Hooper, F. Webber, R. Rao, K. Decker, M. Krein, J. Poleski, R. Barto, and B. Maruyama, "Autonomy in materials research: A case study in carbon nanotube growth," *npj Computational Materials*, vol. 2, no. September, 2016. [Online]. Available: http://dx.doi.org/10.1038/npjcompumats.2016.31

51. O. Drbohlav and M. Chantler, "On optimal light configurations in photometric stereo," *Proceedings of the IEEE International Conference on Computer Vision*, vol. II, pp. 1707–1712, 2005.

52. A. Deraman and P. Layzell, "Software Design Criteria for Maintainability," vol. 3, no. 1, pp. 1–18, 1995.

53. L. Mou and X. X. Zhu, "IM2HEIGHT: Height Estimation from Single Monocular Imagery via Fully Residual Convolutional-Deconvolutional Network," pp. 1–13, 2018. [Online]. Available: http://arxiv.org/abs/1802.10249

REPORT DOCUMENTATION PAGE

Form Approved
OMB No. 0704–0188

1. REPORT DATE *(DD–MM–YYYY)*	2. REPORT TYPE	3. DATES COVERED *(From — To)*
03–21–2019	Master's Thesis	Sept 2017 — Mar 2019

4. TITLE AND SUBTITLE

Non-Contact Height Estimation for Material Extrusion Additive Systems via Monocular Imagery

5a. CONTRACT NUMBER

5b. GRANT NUMBER

5c. PROGRAM ELEMENT NUMBER

6. AUTHOR(S)

Gorospe, Andrew C., Capt, USAF

5d. PROJECT NUMBER

5e. TASK NUMBER

5f. WORK UNIT NUMBER

7. PERFORMING ORGANIZATION NAME(S) AND ADDRESS(ES)

Air Force Institute of Technology
Graduate School of Engineering an Management (AFIT/EN)
2950 Hobson Way
WPAFB, OH 45433-7765

8. PERFORMING ORGANIZATION REPORT NUMBER

AFIT-ENG-MS-19-M-029

9. SPONSORING / MONITORING AGENCY NAME(S) AND ADDRESS(ES)

Air Force Research Laboratory, Materials & Manufacturing Directorate
Dr. B. Maruyama, Leader, Flexible Materials & Processes Research Team
2977 Hobson Way
WPAFB, OH 45433-7733
Email: benji.maruyama@us.af.mil

10. SPONSOR/MONITOR'S ACRONYM(S)

AFRL/RXAS

11. SPONSOR/MONITOR'S REPORT NUMBER(S)

12. DISTRIBUTION / AVAILABILITY STATEMENT

DISTRIBUTION STATEMENT A:
APPROVED FOR PUBLIC RELEASE; DISTRIBUTION UNLIMITED.

13. SUPPLEMENTARY NOTES

14. ABSTRACT

Additive manufacturing is a dynamic technology with a compelling potential to advance the manufacturing industry. Despite its capacity to produce intricate designs in an efficient manner, industry still has not widely adopted additive manufacturing since its commercialization as a result of its many challenges related to quality control. The Air Force Research Laboratory (AFRL), Materials and Manufacturing Directorate, Functional Materials Division, Soft Matter Materials Branch (RXAS) requires a practical and reliable method for maintaining quality control for the production of printed flexible electronics. Height estimation is a crucial component for maintaining quality control in Material Extrusion Additive Manufacturing (MEAM), as the fundamental process for constructing any structure relies on the consecutive layering of precise extrusions. This work presents a computer vision solution to the problem of height estimation using monocular imagery as applicable to MEAM.

15. SUBJECT TERMS

Material Extrusion, Additive Manufacturing, Height Estimation, Monocular Imagery

16. SECURITY CLASSIFICATION OF:			17. LIMITATION OF ABSTRACT	18. NUMBER OF PAGES	19a. NAME OF RESPONSIBLE PERSON
a. REPORT	b. ABSTRACT	c. THIS PAGE			Dr. Gilbert L. Peterson, AFIT/ENG
U	U	U	UU	79	**19b. TELEPHONE NUMBER** *(include area code)* (937) 255-3636, x4281; gilbert.peterson@afit.edu

Standard Form 298 (Rev. 8–98)
Prescribed by ANSI Std. Z39.18